FLOW CHARACTERISTICS OF TRANSLATING FLEXIBLE WINGS AT LOW REYNOLDS NUMBERS

A THESIS SUBMITTED TO
THE GRADUATE SCHOOL OF NATURAL AND APPLIED SCIENCES
OF
MIDDLE EAST TECHNICAL UNIVERSITY

BY

MAHDI YAZDANPANAH

IN PARTIAL FULFILLMENT OF THE REQUIREMENTS
FOR
THE DEGREE OF MASTER OF SCIENCE
IN
AEROSPACE ENGINEERING

AUGUST 2019

Approval of the thesis:

FLOW CHARACTERISTICS OF TRANSLATING FLEXIBLE WINGS AT LOW REYNOLDS NUMBERS

submitted by **MAHDI YAZDANPANAH** in partial fulfillment of the requirements for the degree of **Master of Science in Aerospace Engineering Department, Middle East Technical University** by,

Prof. Dr. Halil Kalıpçılar
Dean, Graduate School of **Natural and Applied Sciences** _____

Prof. Dr. İsmail H. Tuncer
Head of Department, **Aerospace Engineering** _____

Assist. Prof. Dr. Mustafa Perçin
Supervisor, **Aerospace Engineering, METU** _____

Examining Committee Members:

Prof. Dr. Oğuz Uzol
Aerospace Engineering, METU _____

Assist. Prof. Dr. Mustafa Perçin
Aerospace Engineering, METU _____

Assoc. Prof. Dr. Utku Kanoğlu
Aerospace Engineering, METU _____

Assoc. Prof. Dr. M. Metin Yavuz
Mechanical Engineering, METU _____

Assist. Prof. Dr. Onur Baş
Mechanical Engineering, TED University _____

Date: 07.08.2019

I hereby declare that all information in this document has been obtained and presented in accordance with academic rules and ethical conduct. I also declare that, as required by these rules and conduct, I have fully cited and referenced all material and results that are not original to this work.

Name, Surname: Mahdi Yazdanpanah

Signature:

ABSTRACT

FLOW CHARACTERISTICS OF TRANSLATING FLEXIBLE WINGS AT LOW REYNOLDS NUMBERS

Yazdanpanah, Mahdi
Master of Science, Aerospace Engineering
Supervisor: Assist. Prof. Dr. Mustafa Perçin

August 2019, 70 pages

This study experimentally investigates the flow field around surging-translating wings that are started from rest and compares the flow field characteristics with that of surging-revolving wings. Three wings with different level of chordwise flexural stiffness (i.e., highly flexible, moderately flexible and rigid) were studied. The experiments were performed in an octagonal water tank at the Reynold number of 7360 based on the terminal velocity of 0.08 m/s, and the wing chord length of 92 mm. Two-dimensional two-component particle image velocimetry (2D2C PIV) technique was employed to obtain the planar flow fields at the 75% of wingspan position. The PIV measurements reveal a coherent leading edge vortex at the initial phases of the translating motion for all of the wings considered in the study. After approximately two chord lengths of travel, the LEV bursts in the rigid and moderately flexible wings, whereas for the highly flexible wing the LEV preserves its coherency for a longer period of motion. The comparison of flow fields between the translating and the revolving motion kinematics reveals similar behavior of the vortical structures yet the LEV circulation in the translating wings has higher values. The LEV centroid in the revolving cases stays above the leading-edge, while in the translating wings, it always remains at a lower position. The effect of high flexibility results in the retention of LEV closer to the wing surface for both translating and revolving cases.

Keywords: Flexible wings, Particle image velocimetry, Leading edge vortex, Circulation, Flexural stiffness

ÖZ

KÜÇÜK REYNOLDS SAYILARINDA ÖTELEME HAREKETİ YAPAN ESNEK KANATLARIN AKIŞ KARAKTERİSTİĞİ

Yazdanpanah, Mahdi
Yüksek Lisans, Havacılık ve Uzay Mühendisliği
Tez Danışmanı: Dr. Öğr. Üyesi Mustafa Perçin

Ağustos 2019, 70 sayfa

Bu çalışma, durağan durumdan başlayarak doğrusal bir hareket gerçekleştiren kanatlar etrafındaki akış alanını deneysel olarak incelemekte ve akış alanı özelliklerini dönen kanatlarınkiyle karşılaştırmaktadır. Veter yönünde farklı sertlik değerlerine sahip (yüksek esneklikte, orta derecede esnek ve sert) üç kanat incelenmiştir. Deneyler, sekizgen bir su tankında 7360 Reynolds sayında (0.08 m / s son hızına ve 92 mm veter a göre hesaplanmış) gerçekleştirilmiştir. İki boyutlu iki bileşenli parçacık görüntülemeli hız ölçme (2D2C PIV) tekniği, kanat açıklığının %75 indeki konumda düzlemsel akış alanlarını elde etmek için kullanılmıştır. PIV ölçümleri, çalışmada ele alınan kanatların tümü için doğrusal hareketin ilk safhalarında tutarlı bir hücum kenarı girdabı olduğunu ortaya koymaktadır. Yaklaşık iki veter uzunluğu kadar hareket sonrasında, hücum kenarı girdabı sert ve orta derecede esnek kanatlarda bütünlüğünü kaybeder, esnek kanat içinse hücum kenarı girdabı daha uzun bir hareket süresi boyunca tutarlılığını korur. Doğrusal ve döner hareket kinematiği arasındaki akış alanlarının karşılaştırılması, girdap yapıların benzer davranışını ortaya çıkarmaktadır, ancak doğrusal hareket gerçekleştiren kanatlarındaki hücum kenarı girdabı girdaplılığı daha yüksek değerlere sahiptir. Döner kanatlarda girdap merkezi hücum kenarın üstünde kalırken, doğrusal hareket gerçekleştiren kanatlarında daima daha alçak bir

pozisyonda kalır. Yüksek esnekliğin etkisi, hem doğrusal hareket yapan hem de dönen kanatlar için hücum kenarı girdabının kanat yüzeyine daha yakın bir pozisyonda tutulmasına neden olur.

Anahtar Kelimeler: Esnek kanat, Parçacık görüntülemeli hız ölçme, Hücum kenarı girdabı, Girdaplılık, Eğilme sertliği

To my dear parents, Gohartaj and Javad

ACKNOWLEDGEMENTS

First, and foremost, I would like to express my sincere gratitude to my supervisor Assist. Prof. Dr. Mustafa Perçin, who is my role model in my academic life. His kindness, patience, and academic experience are invaluable for me through the years that I worked with him. I appreciate him for introducing this exciting topic to me for my master's thesis. The door to his office was always open whenever I ran into a trouble spot or had a question about my research. Without his enthusiasm, energy, and support, I would not have been able to complete this study.

I would like to extend my deepest gratitude to Prof. Dr. Oğuz Uzol for instructing me the particle image velocimetry technique and for all his support starting from my first day at METU.

I would also like to acknowledge Assoc. Prof. Dr. Bas van Oudheusden of the Faculty of Aerospace Engineering at Delft University of Technology for all his support and sending us flexible wing materials which I used in my study.

I would like to appreciate Dr. Human Amiri for his help and advice in setting up my experiments and thank Dr. Saffet Gökuç and the department technician Ahmet Uyar, for all their help in my experiments.

I want to thank Dr. Nima Shojaee, Mahdi Saeedi Nikoo, Majid Ghaderi, Hadi Javani, Lina Jurkunas, Monir Habibi, Serkan Yener, and Beyza Avan for their support and encouragement.

Finally, I would like to express my eternal gratitude to my parents, Gohartaj and Javad, for their love and support throughout my life.

TABLE OF CONTENTS

LIST OF TABLES

TABLES

LIST OF FIGURES

FIGURES

LIST OF ABBREVIATIONS

2D 2C	Two-dimensional two-component
2D PIV	Two-dimensional particle image velocimetry
CCD	Charge-coupled device
AR	Aspect ratio
FOV	Field of view
LE	Leading edge
LEV	Leading edge vortex
PIV	Particle image velocimetry
TE	Trailing edge
TEV	Trailing edge vortex
Nd:YAG	Neodymium-doped yttrium aluminum garnet ($Nd:Y_3Al_5O_{12}$)
PET	Polyethylene terephthalate

LIST OF SYMBOLS

γ_1, γ_2	Two-dimensional vortex location, size detection criterion
α	Angle of attack [*deg*]
Γ	Circulation [m^2/s]
Γ^*	Dimensionless circulation
δ^*	Chord length of travel
ω	Vorticity [$1/s$]
ρ	Density [kg/m^3]
c	Chord [m]
t	Time [s]
E	Young's modulus [N/m^2]
h	Thickness [m]
I	Area moment of inertia [m^4]
EI	Flexural stiffness [Nm^2]
Π_1	Stiffness parameter
υ	Poisson ratio
V_t	Terminal velocity [m/s]
x,y,z	Directions [m]
L/D	Lift to drag ratio
C_L	Lift coefficient
C_D	Drag coefficient

CHAPTER 1

INTRODUCTION

Nature has been a great source of motivation in the design and development of airborne machines for centuries. Recently, with the advent of micro air vehicles (MAVs), many researches focus on the flapping flight of biological flyers since fixed and rotary wings become inefficient in the typical low Reynolds number (Re) regime of MAV operation (Pines and Bohorquez, 2006). Figure 1.1 shows the maximum lift coefficients (C_{Lmax}) versus the corresponding Reynolds numbers in different experiments from smooth airfoils in a steady flow to hovering insects in an unsteady flow.

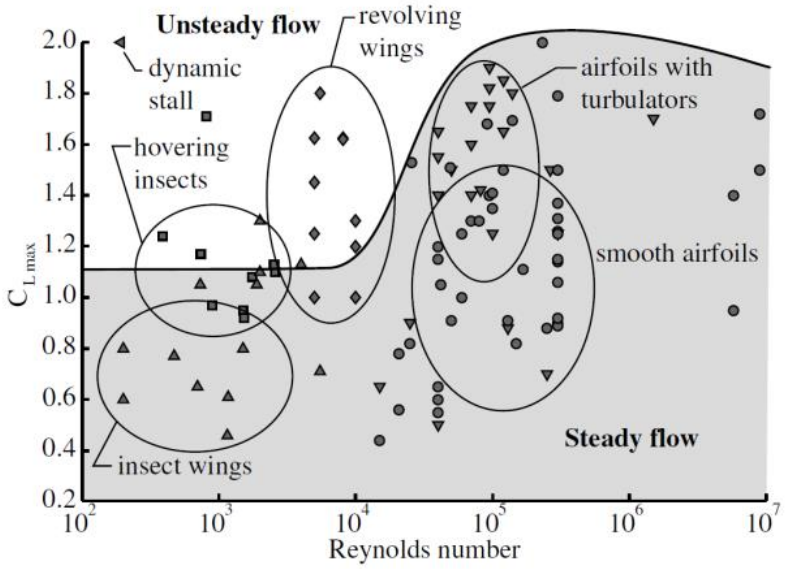

Figure 1.1. $C_{L\,max}$ of different studies in steady and unsteady flows versus Reynolds number reported in the literature (Jones and Babinsky, 2010)

The shaded area in Figure 1.1 represents experiments (airfoil with turbulators, insect wings and, smooth airfoils) in a wide range of Reynold number. It can be found that at high Reynolds number steady flows, smooth airfoils perform reasonably well; however, at low Reynolds numbers, the performance declines even when insect wing geometries are used in the experiments. As mentioned above, conventional means of force generation (rotary and fixed wings) have low C_{Lmax} values at the low Reynolds numbers and therefore, studying flapping wings at low Reynolds numbers is a necessity to sustain the progress in the field of micro air vehicles. Hovering insects and revolving wings are experiments in unsteady or three-dimensional flow and they are shown in the white area in Figure 1.1.

A stable leading edge vortex (LEV) has shown to be one of the most prominent force generation mechanisms (Ellington et al., 1996). It has been subject to numerous investigations, and different hypotheses have been put forward regarding its stability, such as spanwise advection of vorticity (Ellington et al., 1996), tip vortex inducing a downward flow and inhibiting the growth of the LEV (Birch and Dickinson, 2001), or the apparent rotational (Coriolis and rotational) accelerations in the low Rossby number regime (Lentik and Dickinson, 2009). The latter hypothesis has also been in a good agreement with the studies of Jardin and David (2014, 2015) in which they showed that the enhanced aerodynamic performance is ensured by the apparent Coriolis effect while the LEV attachment can be achieved by the spanwise advection of vorticity.

The flapping wing motion can be decomposed into three motion kinematics: sweeping, plunging and pitching. In the literature, the sweeping motion is simulated by either a rectilinear translation (i.e., infinite Rossby number) or revolving motion (finite Rossby number). The latter is a more realistic representation of the actual case due to the occurrence of rotational accelerations, which, as aforementioned, are considered to be the effective factor in the attachment of the LEV. To study comprehensively the flapping-wing aerodynamics, it is common to investigate individual motions to understand fundamental mechanisms of each motion.

Flapping-wing phenomenon in realistic configurations is further complicated by the presence of wing flexibility, which is an aspect often neglected in mechanical simulations. Wing flexibility has been shown to be an effective factor in increasing the aerodynamic performance in different studies (Shyy et al., 2010). Zhao et al. (2010) showed that flow structures are similar for different wing flexibilities, yet the size of the LEV is influenced by the flexural stiffness. Beals and Jones (2015) considered a flexible revolving wing in the Re range from 10000 to 25000. The flexible wing generated less lift comparing to the rigid wing, yet the deformation of the wing mitigated the negative effects of wake encounter.

The objective of this thesis is twofold:

1. To investigate the effects of rotational mechanisms that are responsible for the stability of the LEV for chordwise-flexible wings by means of comparing two motion kinematics surging translational motion and surging revolving motion;
2. To investigate the effects of wing flexibility on the LEV and flow field characteristics.

For these purposes, 2D2C-PIV measurements were performed around rigid and flexible wings that undergo a linear translational motion starting from rest. Two flexible wings with different flexural stiffness values were compared to one rigid wing.

The results of this study are compared to that of a master's thesis study in the Faculty of Aerospace Engineering of Delft University of Technology (TUD) in which the revolving motion is considered for the sweeping motion and three-dimensional (3D) flow characteristics of flexible revolving flat plates were investigated by employing tomographic particle image velocimetry (Tomographic-PIV).

This document is divided into five chapters. An introduction and overview of the literature are given in Chapter 1. Chapter 2 details the literature regarding the flapping-wing aerodynamics, and Chapter 3 describes the experimental setup. In Chapter 4, the

results of this study are explained and discussed, and lastly, the main conclusions of this thesis are given in Chapter 5.

CHAPTER 2

FLAPPING-WING AERODYNAMICS

In this chapter, the unsteady mechanisms which play the roles in flapping-wing aerodynamics are introduced and summarized. The aerodynamic phenomena which occur during sweeping motion in flapping flight, and can be expressed by a surging translating/revolving wing model are discussed in more detail. At the end of this chapter, more information about flexible wings are given.

2.1. Unsteady Mechanisms in Flapping-Wing Flight

Natural flyers (insects, birds, bats, etc.) often have flapping-wing motion to fly forward/backward and hover in air. Three-dimensional effects which occur for small aspect ratio wings at low Reynolds numbers can characterize the aerodynamics of flapping wings. In Figure 2.1, The schematics of primary kinematics for flapping wing motion is shown.

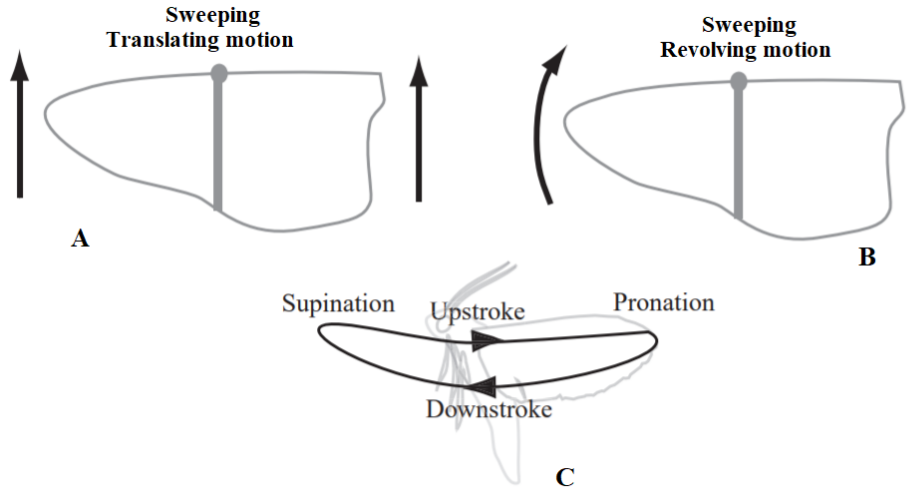

Figure 2.1. Primary kinematics for the sweeping motion during the flapping flight (Sane, 2003)

Figure 2.1-A shows translating motion in which the tip of the wing moves together with the wing root, and B represents the revolving motion in which the wing tip revolves around the fixed point in the root. As aforementioned, biological flyers move their wings in 3D motions which can be decomposed as sweeping, plunging and pitching (Supination and pronation). Sweeping motion is fore and aft movement of the wing, and plunging is the up and down motion of the wing. Figure 2.1-C shows the phases of a biological flyer's flapping motion kinematics. The wing pronates and supinates at the end of each half stroke. During the upstroke and downstroke phase, plunging and sweeping motions occur concurrently. Some force generation mechanisms related with aerodynamics of flapping flight are as follows:

1. Clap and fling motion
2. LEV and retarded stall (delayed stall)
3. Rotational forces
4. Added mass
5. Wake capture effect

2.1.1. Clap and Fling Motion

Clap-and-fling is a motion which enhances the lift generation as a result of wing-wing interference and was first introduced by (Weis-Fogh, 1973). Figure 2.2 represents the phases of the clap and fling motion. In Figure 2.2, the direction of the wing motion and the induced flow are indicated by red and blue arrows, respectively, and the black lines indicate the flow lines. In the clapping phase at the end of upstroke, first the wings leading edges become close to each other (Figure 2.2-A), and at this transition phase, the pronation occurs (B and C). In section C, the fluid is pushed out by closing gap between two wings, resulting in more thrust force. The flinging phase occurs from D to F where at F, the wings rotate around the trailing edges, and the flow is sucked to the gap between the wings. In subsequent sections, the two wings move apart from each other.

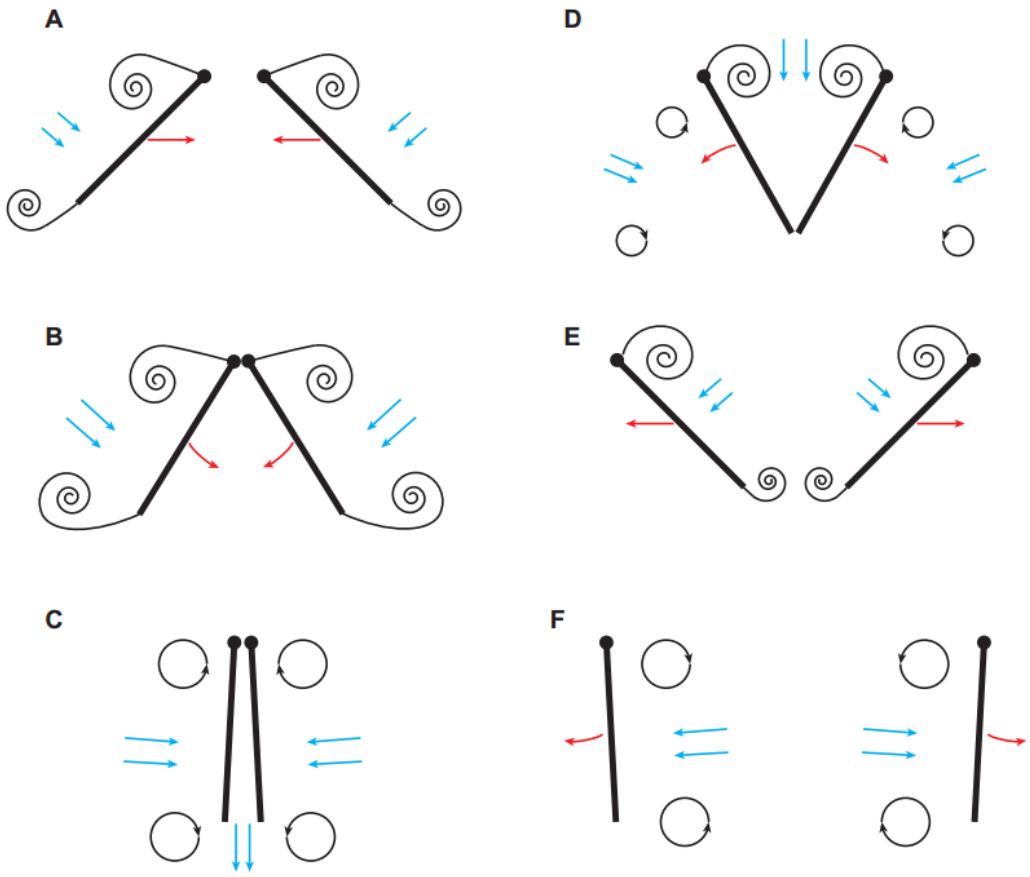

Figure 2.2. Schematics sections of clap (A to C) and fling (D to E) (Percin, 2015)

The wing flexibility has a great influence on clap and fling motion at which the fling motion is more like a peel (Ellington, 1984). Miller and Peskin (2009) showed that clap and fling motion in flexible wings leads to the generation of lower drag values and greater lift values compared to rigid wings, which results in L/D enhancement.

2.1.2. Leading edge Vortex and Delayed Stall

LEVs are considered as an important factor in the force generating mechanisms by providing a low-pressure region in the suction side of the wing. Muijres et al. (2008) showed that LEVs can produce 50% of the lift on the wing.

In sweeping motions, the flow separates from the leading edge if the angle of attack is relatively high. The flow reattaches to the surface of wing and leaves the trailing edge tangentially. In this case, the Kutta condition preserves, and the more wing continues to its rectilinear translating motion, the more momentum is conveyed to fluid in the downward direction, which increases the lift generation. Figure 2.3 represents a comparison between the flow around a wing in translating and revolving motions.

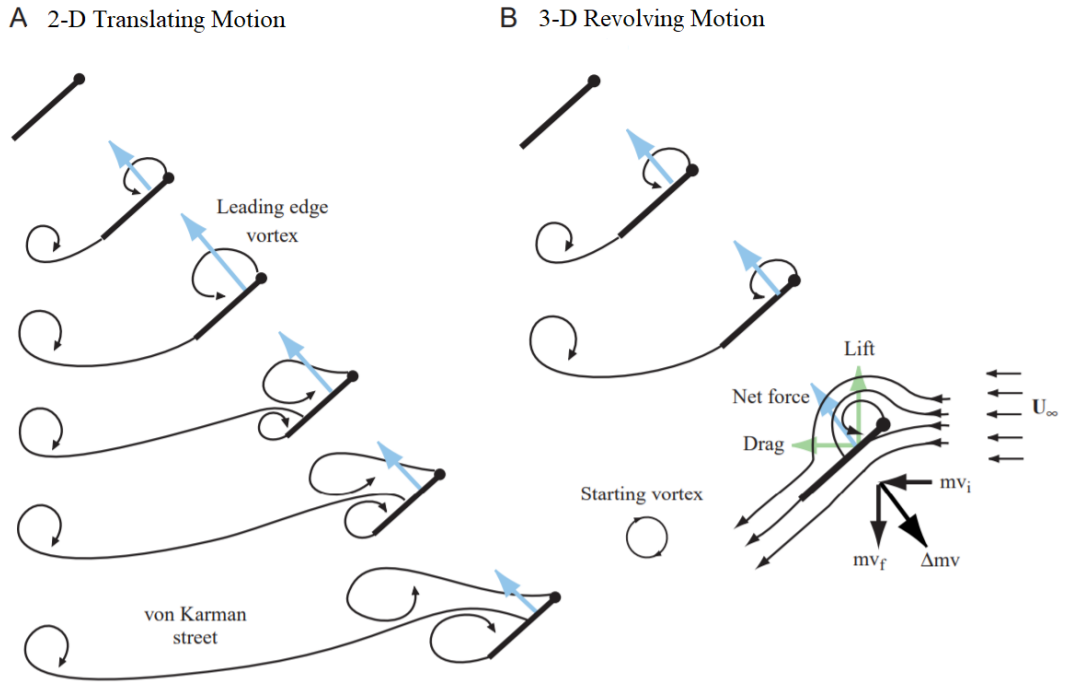

Figure 2.3. A comparison between translating and revolving motions (Sane, 2003)

For translating motion (2-D motion), if the wing translates with a large angle of attack, the flow separates at the wing leading edge, forming a LEV. If the wing travels more, the trailing edge vortex (TEV) sheds to the wing wake. This is followed by the growth of LEV according to Kelvin's circulation theorem. Kelvin's circulation theorem states that the circulation around a closed curve moving with the fluid remains constant with time. Thus, to maintain constant circulation value, the LEV grows as the TEV sheds

to the wing wake. In the translating motion, the LEV cannot remain attached, and it sheds to the wake. When the Kutta condition fails, the wing cannot convey a steady momentum to the fluid particles in downward direction, lift drops significantly and the wing stalls. The stable LEV produces remarkably great lift before the stall occurs, and this situation is called as 'delayed stall' (Sane, 2003).

A new LEV forms as the TEV detaches and sheds into the wake and this process repeats which forms a wake region of counter-rotating vortices known as the 'von Karman vortex street.' The forces (lift and drag) have the highest values in phases when a stable LEV is present above the wing. According to Figure 2.3, in a revolving wing motion (3-D motion) starting from the rest, a LEV is generated; however, the LEV does not shed after sweeping for many chord lengths, and thus a similar pattern to a von Karman street cannot be created. In contrast to translating motions, a spanwise flow is present in revolving motions. As the wing revolves, the LEV interacts with a spanwise flow which leads to the spiral flow from root to tip (Sane, 2003). The LEV for a revolving wing and the downwash flow by cause of the vortex around the wing are depicted in Figure 2.4.

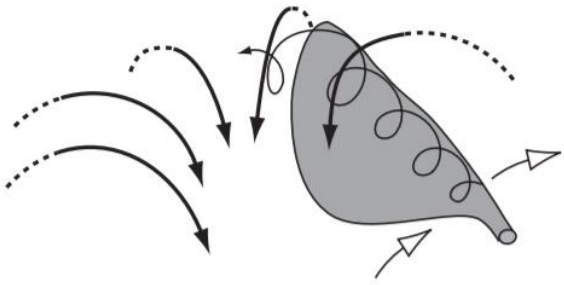

Figure 2.4. LEV for revolving wing and downwash (Vandenberg and Ellington, 1977)

The axial flow changes the direction of momentum transfer to the spanwise direction leading to the LEV attaining a constant size (Figure 2.3-B). As a result of the spanwise advection of vorticity, no new vorticity is formed at the trailing and leading edges, following in the attached LEV throughout the revolving motion. In this condition, the

Kutta condition is obeyed, and it confirms that the direction of momentum changed from the horizontal direction to the downward direction. In the Figure 2.3-B, mv_i, mv_f and Δmv represent the initial momentum, the final momentum and the difference between the two momenta, respectively. When the Kutta condition holds for a revolving wing, the net aerodynamic forces remain stable over a period during the revolving. For Re numbers greater than 100 in a revolving motion, the net aerodynamic force is generated perpendicular with respect to the wing upper surface (Sane, 2003).

Lentik and Dickinson (2009) experimentally investigated the stability of leading edge vortices. They studied the dynamically scaled model of Drosophila melanogaster undergoing the translating and revolving motions in two different Reynolds numbers. They showed that LEV sheds in the translating motion, whereas it remains attached in the revolving motion.

2.1.3. Rotational Forces

As a revolving wing rotates about a spanwise axis while concurrently performing a sweeping motion, the flow around the wing digresses from Kutta condition, and as a result, the stagnation point detaches from the trailing edge. This leads to shear due to the sharp gradient of velocity. Since the viscosity of the fluid causes the resistance to shear, additional circulation is needed to reestablish the Kutta condition at the trailing edge. In summary, the wing generates extra circulation proportional to the angular velocity of revolving to counteract the rotational effects in order to establish smooth, tangential flow at the wing trailing edge. Based on the direction of rotation, this additional circulation creates rotational forces that can affect the net force generation of the wing (Sane, 2003).

2.1.4. Added Mass

Circulatory forces are the force generation mechanisms that affect the circulation around the wing (LEV, clap and fling motion, and rotational forces). Added mass effect, which is also called as an acceleration reaction (Denny, 1993) is a non-

circulatory effect. When a wing starts to accelerate, the fluid around the wing is also accelerated, and this results in the reaction force to the wing, generated by the accelerated fluid. This reaction force can be considered as a growth in the inertia of the moving object as a result of the accelerated fluid mass or so-called added mass (Percin, 2015).

2.1.5. Wake Capture Effect

Figure 2.5 represents the time sequence of the wake capture mechanism. At the end of each half stroke, the wing pronates and supinates to start a new stroke, and the wing interacts with the counter-rotating shed vorticity present in its own wake during each stroke. A strong velocity field is induced by these regions of vortices (Figure 2.5-C and D). The wing extracts energy from the wake, which increases aerodynamic forces (Figure 2.5-E). This phenomenon is also called as wing-wake interaction or wake capture.

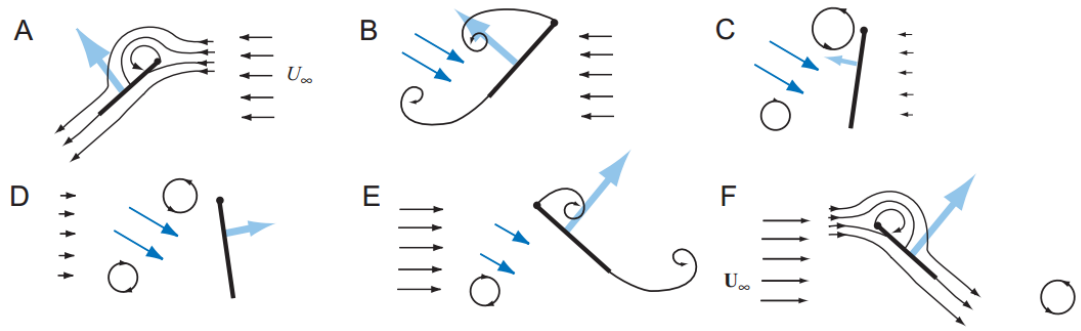

Figure 2.5. The time sequence of wake capture (Sane, 2003)

The effect of wing-wake interaction completely depends on two factors, the wake vorticity magnitude and its orientation in stroke reversal (Birch and Dickinson, 2003), and the wing kinematics can affect these two factors. The wings interact with their wake during the hovering flight which increases the lift generation; however, in the advancing flight, due to advection of wake structures, wing-wake interaction will not occur. Biological flyers can adjust the fluid speed and accelerated mass by increasing

or decreasing the stroke frequency and amplitude, which influence on the kinetic energy available in the wake (Sane, 2003).

2.2. Lift and Thrust Generation in the Forward Flight

Biological flyers generate both lift and thrust as a helicopter rotor generates but there are some differences in their mechanisms. The helicopter has continuous rotation and rotation is not a movement that is available in nature to be produced by muscles; so instead, biological flyers produce reciprocal motion, which is possible to do with their muscles. Helicopters tilt their nose and rotor forward to have advancing flight, whereas birds and insects incline the flapping stroke plane. Figure 2.6 illustrates the stroke plane for hovering and forward flight.

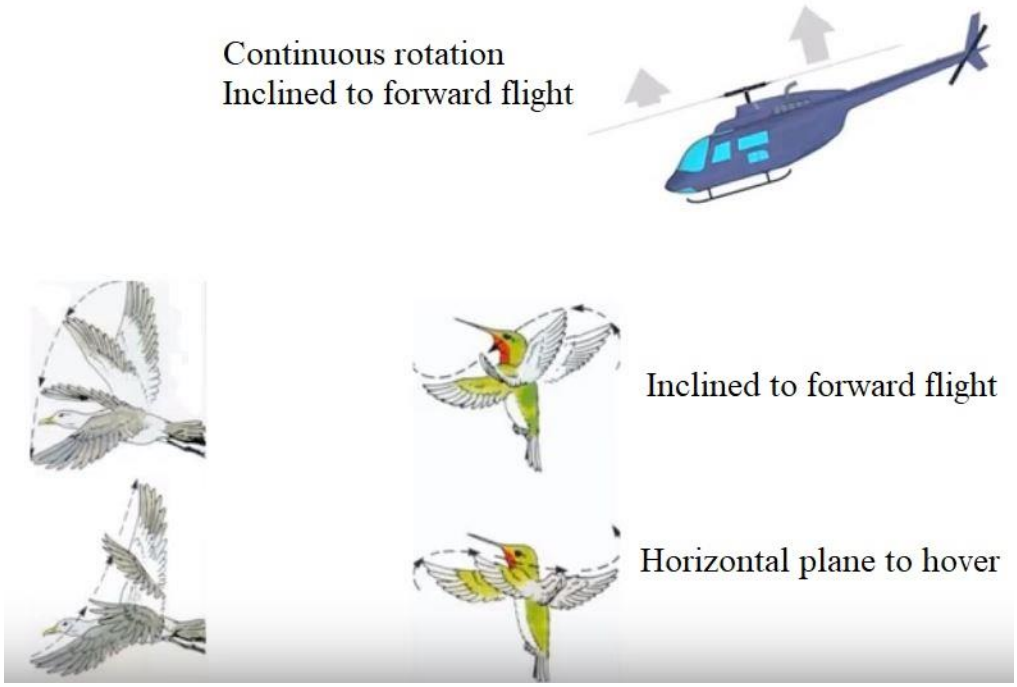

Figure 2.6. Stroke planes in hover and advancing flight (Alexander, 2002)

Tips of the wing in the flapping stroke trace either an inclined ellipse or a figure of eight, and it can be differentiated in two phases: the downstroke and the upstroke.

Figure 2.7 shows the downstroke and upstroke in the forward flight (Alexander, 2002). There are very complex strokes in nature for some insects with complicated patterns and loops, and some examples are given in Figure 2.8.

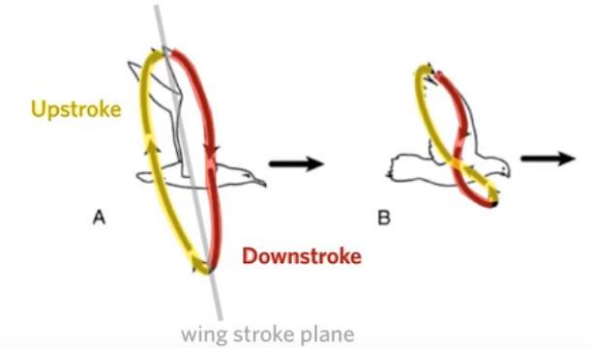

Figure 2.7. Downstroke and upstroke in the forward flight (Alexander, 2002)

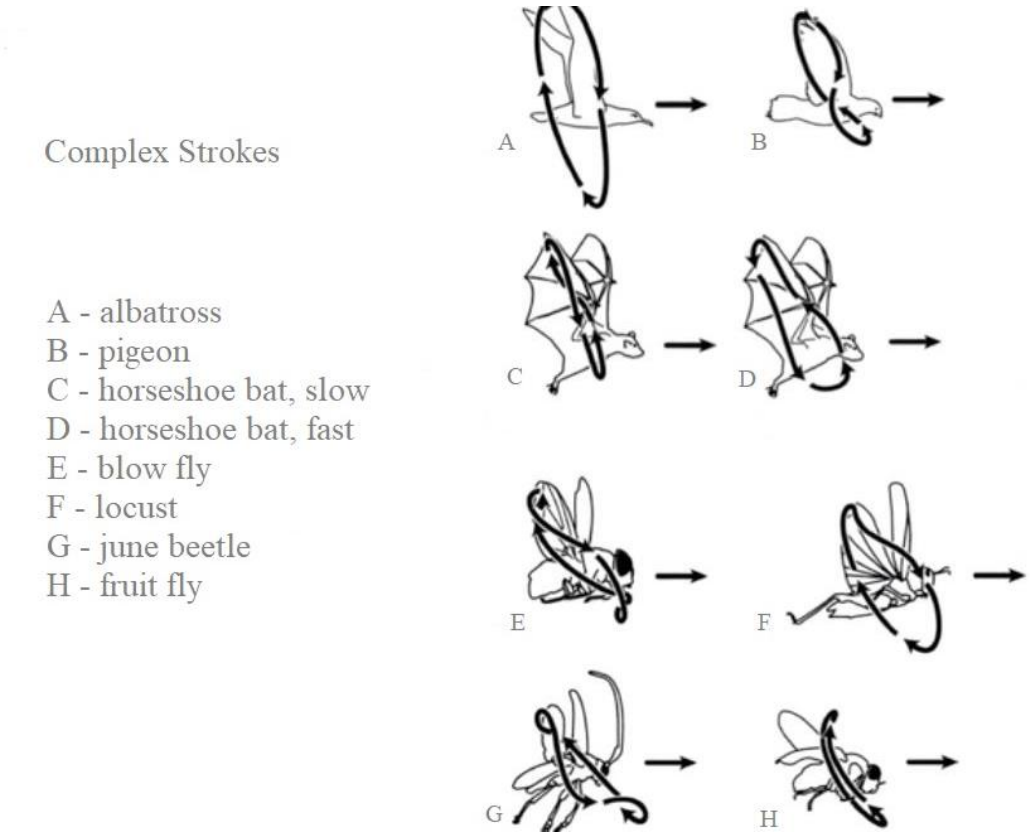

Figure 2.8. Complex flapping strokes in nature (tip of the wing) (Alexander, 2002)

The schematics of forces and airflow in the downstroke phase of a flapping stroke in a forward flight are shown in Figure 2.9.

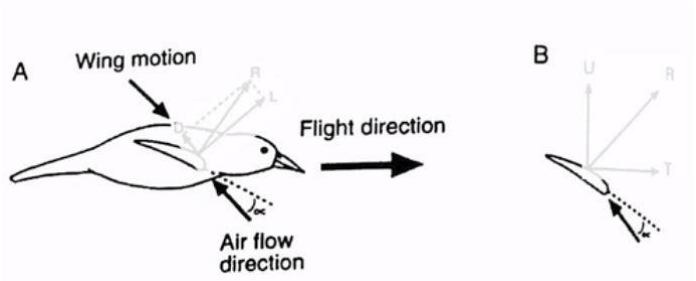

Figure 2.9. Downstroke phase in the forward flight. (A) flow direction. (B) resultant force (Alexander, 2002)

In Figure 2.9-A, the wing is moving downward, which results in the upward velocity of air, and the bird is moving forward, resulting in the air flow towards the wing. These two air flows adapt to the relative wind with respect to the wing shown with an arrow and an angle of attack in the figure. The lift and drag forces are always generated perpendicular and parallel to the flow direction, respectively. The resultant aerodynamic force (R) is the vector sum of lift and drag, as shown in the Figure 2.9-A. The resultant force is redrawn in Figure B, and it can be decomposed in two forces; the horizontal component (T) is the thrust which overcomes drag on the bird and the vertical component (U) is the actual lift opposing the weight of the bird. In the upstroke phase or recover stroke, the biological flyers reduce the angle of attack for having fast flight and during the upstroke, the wings generate negative thrust; however, the aerodynamic force is much less (Alexander, 2002).

2.3. Revolving-Translating Wings in Pitching and Surging Condition

There were several studies exploring the force generation and flow field around the wings undergoing revolving and translating motions in surging and pitch up conditions. Ol and Babinsky (2016) reviewed two different studies from University of Maryland and TU Delft in which they compared the lift coefficient and flow fields around the rigid flat plates in those cases. The two studies include surging translating,

surging revolving and pitching translating conditions. The translating wings had an aspect ratio of 4 and revolving wings had an aspect ratio of 2. In all cases, the motion kinematics included an acceleration phase and a constant velocity phase. They tested the wings in two different accelerating conditions, the fast acceleration and the slow acceleration. Thus, in the translating cases, they performed tests on fast pitch, fast surge, slow pitch, and slow surge conditions. The flow field (velocity vectors and vorticity) around the translating flat plates in different conditions for different chord lengths of travel (s/c) at 75% of span position, from University of Maryland group results are illustrated in Figure 2.10. The flow fields over the revolving flat plates in fast surge and slow surge conditions at 50% of the span position from TU-Delft and University of Maryland groups results, are given in Figure 2.11.

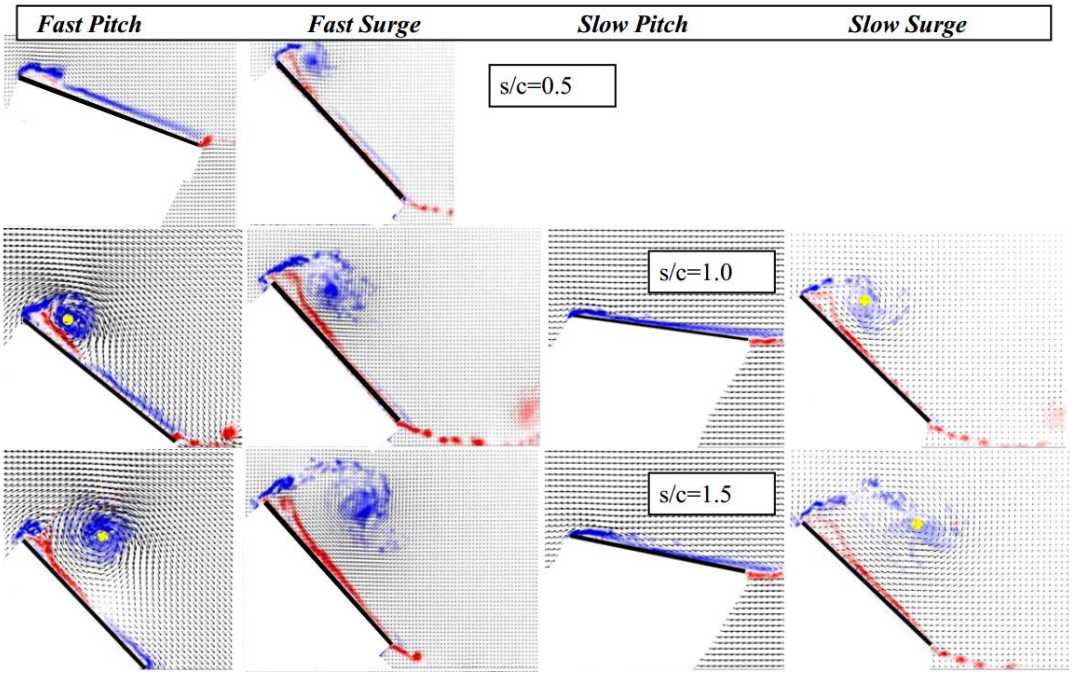

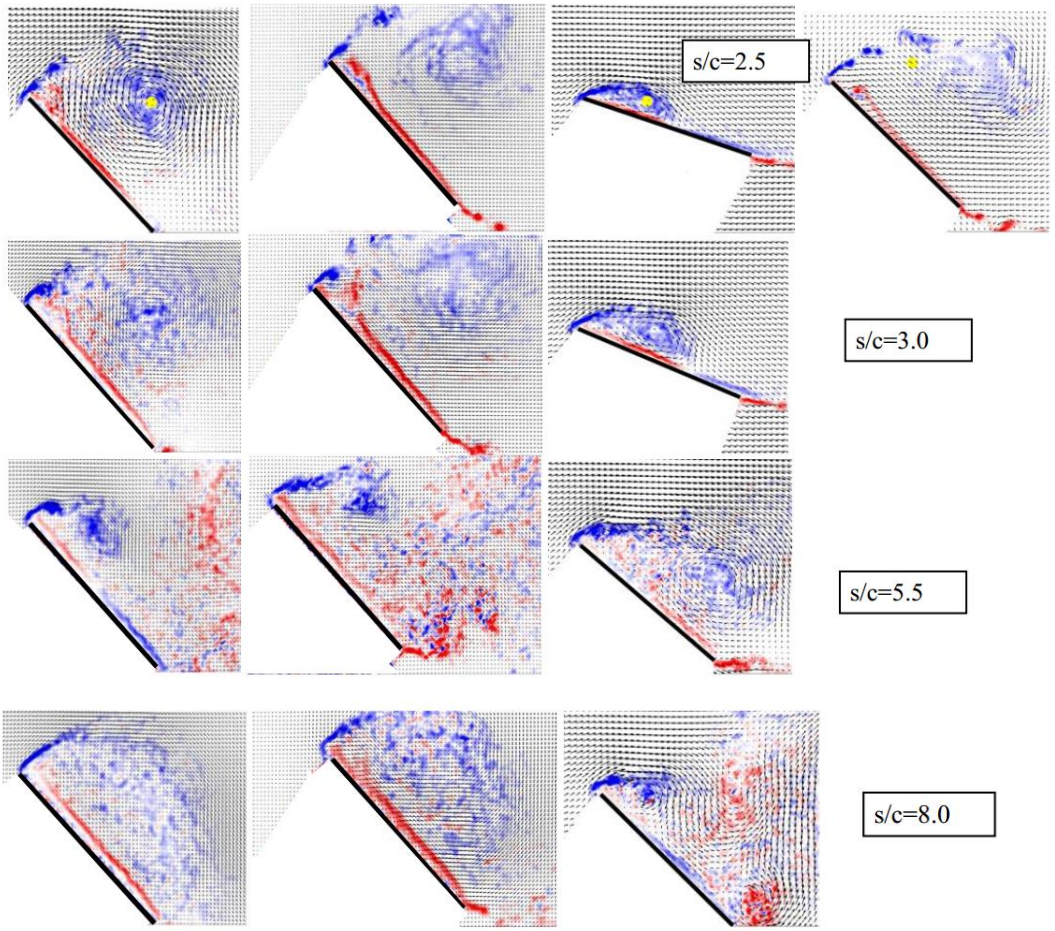

Figure 2.10. Velocity vectors and vorticity contours of translating flat plates at 75% of span position for four different conditions at different chord lengths of travel (Ol and Babinsky, 2016)

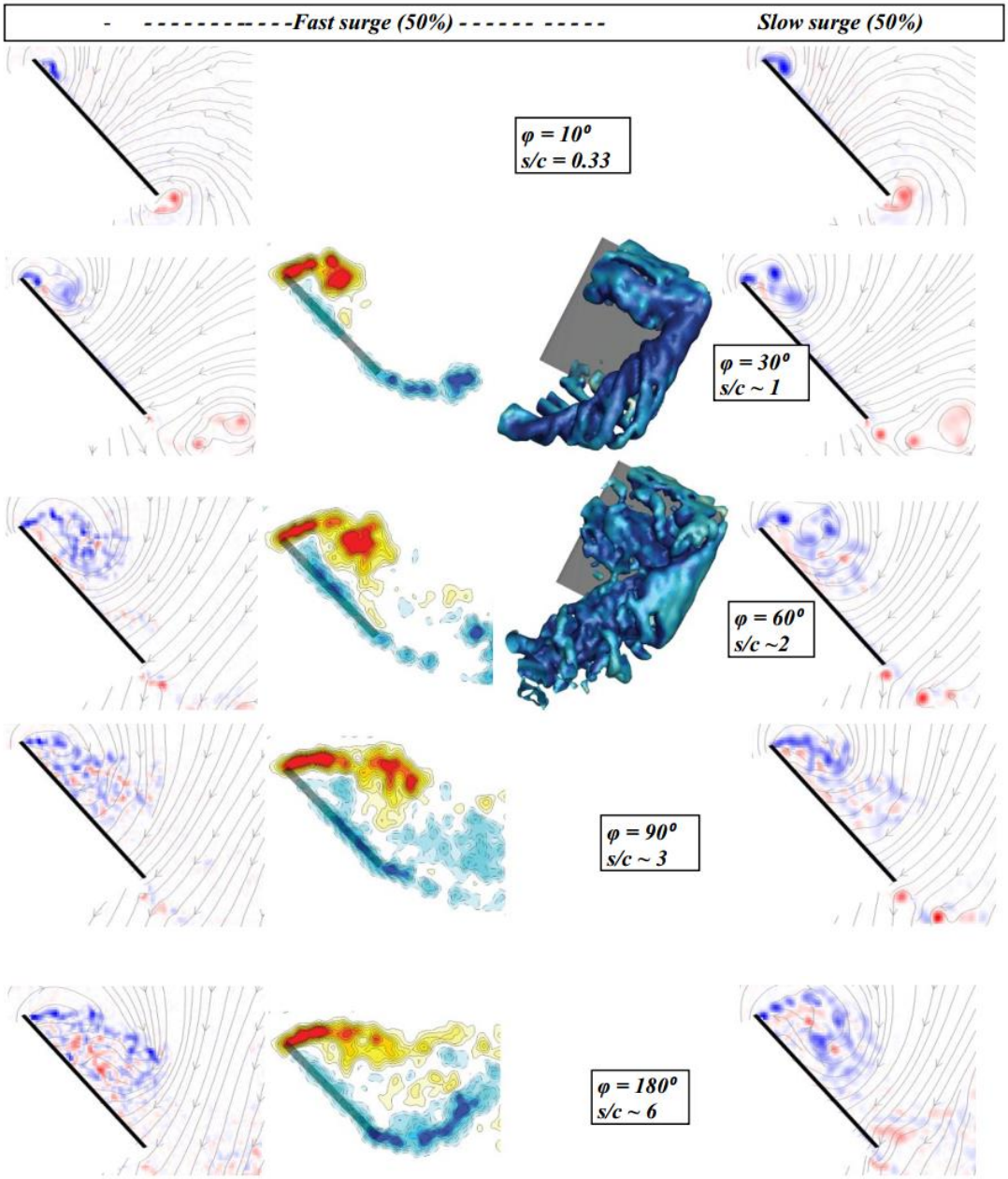

Figure 2.11. Streamlines and out-of-plane vorticity contours of surging-revolving flat plates at 50% of span position for fast and slow surging conditions at different chord lengths of travel. The first three lists, left to right are fast surge and the right most list is representing slow surge. The second and third columns are from TU Delft results (Ol and Babinsky, 2016)

The most important difference between the Figure 2.10 and 2.11 is the LEV stability. They showed that all different motion and cases generate similar LEV in terms of strength and behavior.

They compared the lift coefficient generated by surging wings in revolving and translating motions in different studies from multiple research groups and different participating laboratories. The temporal evolution of lift coefficient for fast surging-translating and surging-revolving cases is show in Figure 2.12.

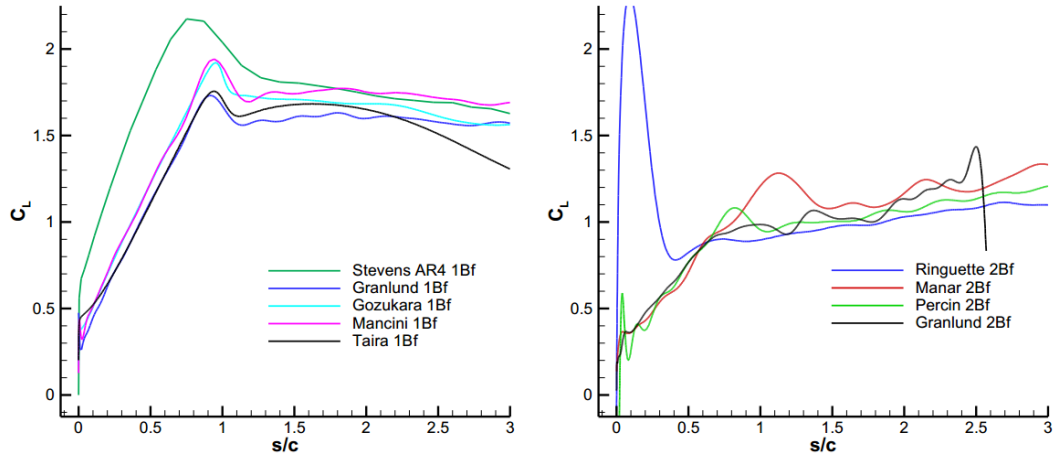

Figure 2.12. Temporal evolution of C_L for fast surging-translating wings (left) and fast surging-revolving wings (right) at α=45° (Ol and Babinsky, 2016)

Figure 2.12 shows similar rise in lift generation in the acceleration phase in both motions; however, there are two differences in subsequent stages. The translating wings generate constant lift values lower than the peak value in the acceleration phase, while in the revolving wings, the lift coefficient increases to higher values which shows the persistence of stable LEV. In addition, they showed that the fast pitch conditions generate a larger lift than fast surge conditions.

They compared the normalized LEV circulation from different AVT-202 contributors (Figure 2.13) for translating-surging and translating-pitching wings with the Wagner's theoretical curve (Wagner, 1925).

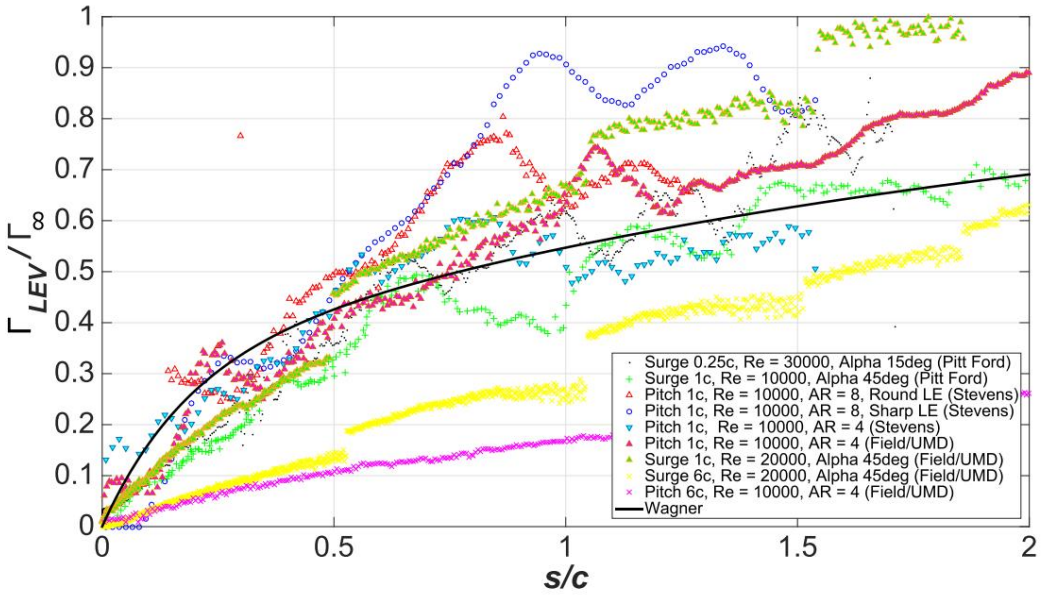

Figure 2.13. Normalized LEV circulation for translating-surging and translating-pitching rigid wing from different contributors of AVT-202 group (Ol and Babinsky, 2016)

They showed that the LEV circulation does not follow the Wagner's curve. They showed that LEV moves away from the leading edge with a speed lower than free stream speed, while the TEV moves with a speed close to the flow stream speed.

2.4. Flexible Wings

Nature's flyers, in reality, have flexible wings which due to the complexity of fluid-structure interferences are difficult to model. The wing deforms due to the viscous stresses and pressure created by the fluid flow which the dominant parameter is the pressure. This deformation of the wing influences the flow around the wing again. A moving boundary problem occurs under the influence of the flow around the boundary of the wing. Combes (2003) showed that for Nature's flyers, the wing size is a ruling factor in the calculation of flexural stiffness (*EI*). They also showed that the spanwise flexural stiffness is almost 10 to 100 times greater than chordwise flexural stiffness.

2.4.1. Effect of Wing Flexibility

Wing flexibility has been shown to be an effective factor in increasing the aerodynamic performance of flapping wings in different studies (Shyy et al., 2010); however, the experimental studies on revolving-translating flexible wings need to be investigated more to explore wing flexibility effects on force generation and flow field around sweeping wings. Zhao et al. (2010) investigated the results of flexibility in the chordwise direction on the aerodynamic performance of different wings having different flexible materials undergoing the steady-state revolving motion. They performed the experiments at different angles of attack at a Reynold number of 2000. Different wing models had different flexural stiffness values by having different materials and thicknesses. The force coefficients for different angles of attack are given in Figure 2.14. It was reflected that for angles of attack less than 45 degrees, the lift decreases as the flexural stiffness decreases in the revolving wings. However, for angles of attack more than 45 degrees, the rigid wings (high flexural stiffness) have a decrease in the lift generation compared to the flexible wings (particularly those with low flexural stiffness) which showed more or less a constant lift generation.

The maximum lift is generated at $\alpha = 45^{\circ}$ for a rigid wing, while for the flexible wings, depending on the flexural stiffness, the maximum lift can be generated at different angles of attack. Figure 2.14 reveals that the aerodynamic force generation decreases as the wing's flexural stiffness decreases, and rigid wings generate greater lift and drag compared to flexible wings. Zhao et al. (2010) showed that the flow structures are not changed by wing flexibility; however, the LEV size is smaller for flexible wings which agrees with the generation of aerodynamic forces; as the LEV size becomes smaller, the aerodynamic forces decrease.

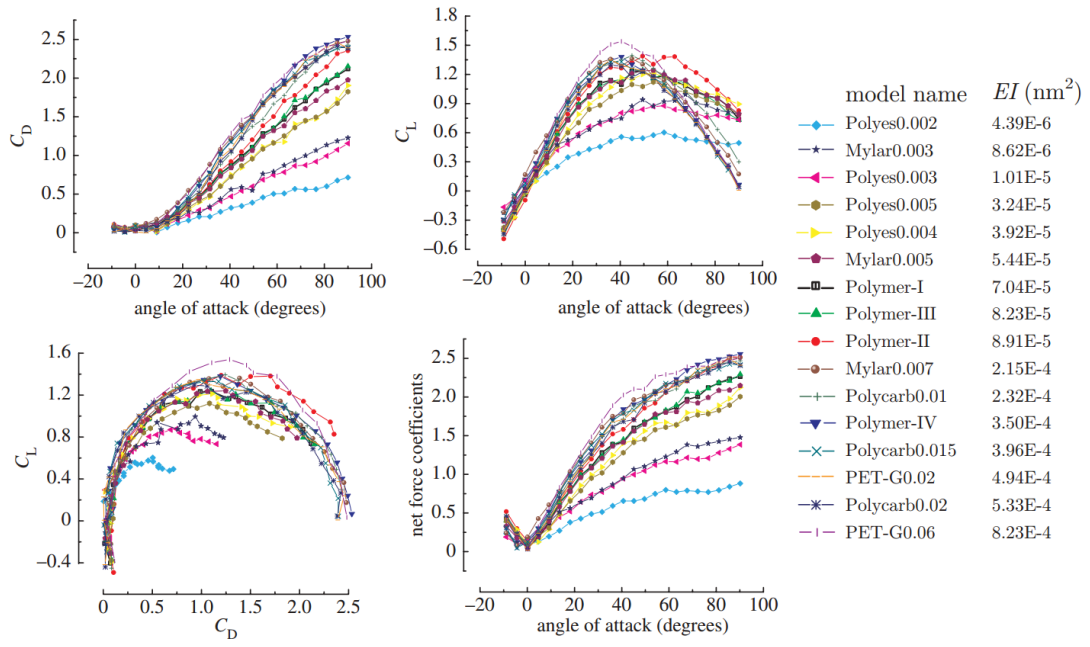

Figure 2.14. Force coefficients for different angles of attack for different flexible wings (Zhao et al., 2010)

There was another study by Beals & Jones (2015) who studied a rigid wing and a chordwise flexible wing made of two rigid boards attached at the mid-chord undergoing a revolving motion for different Reynolds numbers from 10000 to 25000. The rigid wing generates more lift compared to the flexible one; however, passive wing deformation in the flexible wing results in the mitigation of the lift losses during the wake encounter.

Wing flexibility is assumed to be an effective factor in increasing the aerodynamic performance in the flapping motion in some studies (Mountcastle and Daniel, 2009; Eldredge et al., 2010).

Van de Meerendonk et al. (2018) studied wings undergoing surging-revolving motion in an octagonal water tank. A virtually rigid plate was built from 1 mm thick Plexiglass whereas the moderately flexible and highly flexible wings were built from Polyethylene terephthalate (PET) with thickness values (h) of 175 μm and 125 μm,

respectively. The temporal evolution of the lift and drag coefficients (C_L and C_D, respectively) for the three wings tested in these experiments are shown in Figure 2.15. Both lift and drag decreases with decreasing flexural stiffness, yet the decrease of drag is much greater than that for lift. In Figure 2.15, lift-to-drag ratio is given and we can observe that due to the relatively high decrease in drag than lift for decreasing flexural stiffness, lift to drag ratio increases for highly flexible flat plate, and these results reveal that the wing flexibility enhances the aerodynamic performance (L/D) in the revolving-surging flexible wings.

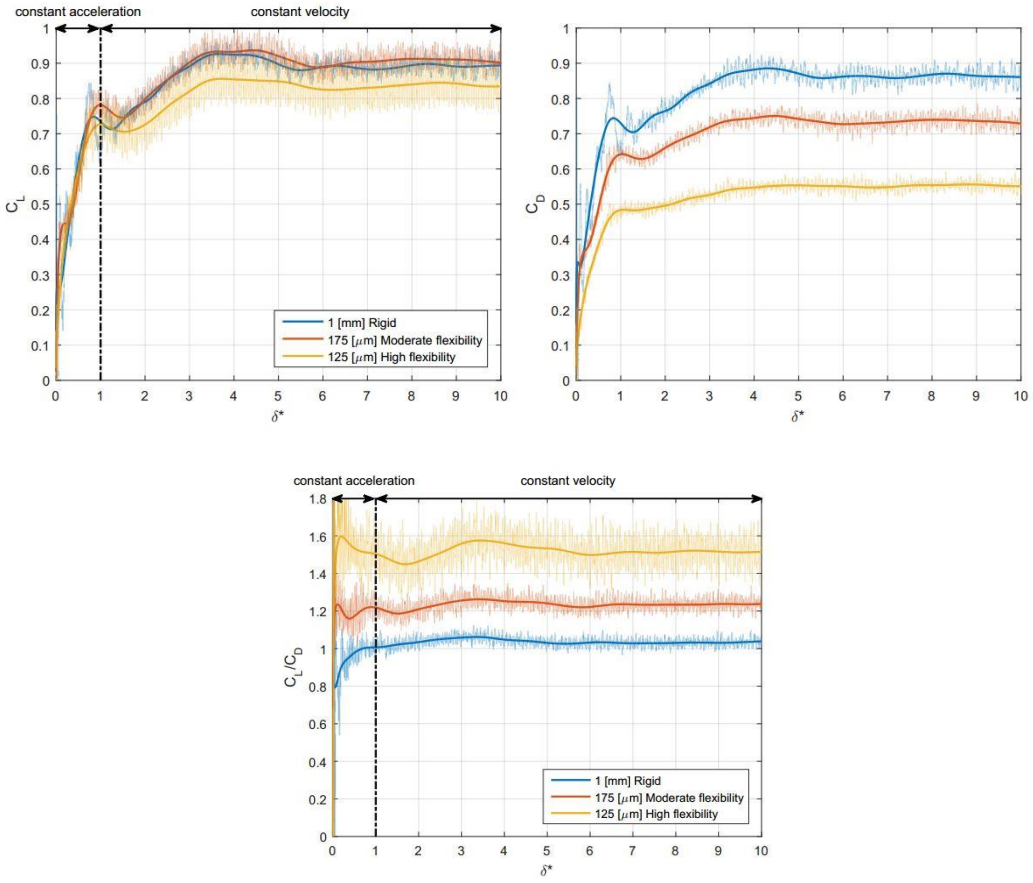

Figure 2.15. Temporal evolutions of lift coefficient (up-left), drag coefficient (up-right) and L/D for the studied revolving-flat plates (bottom) (van de Meerendonk et al. 2018)

CHAPTER 3

EXPERIMENTAL METHODS

3.1. Water Tank

The translating wing measurements were conducted in an octagonal water tank (Figure 3.1) at the Aerodynamic Laboratory of the Aerospace Engineering Department of Middle East Technical University. The dimensions of the tank are 1m × 1.5 m (distance between parallel edges × height), and it is made of glass to have an optical access for imaging and laser illumination.

Figure 3.1. Water tank

The wing models are driven by a robotic arm placed above the tank. The robotic arm has three degrees of freedom (translating in the x and y-axis and 360° of rotation around the z-axis, see Figure 3.2). The desired motion kinematics can be programmed in the control unit of the driving system. There is an integrated camera board on which the PIV cameras can be placed. The integrated camera board moves with the robotic arm, thus the flow field in all PIV images are the same. The robotic arm and control unit are shown in Figure 3.2.

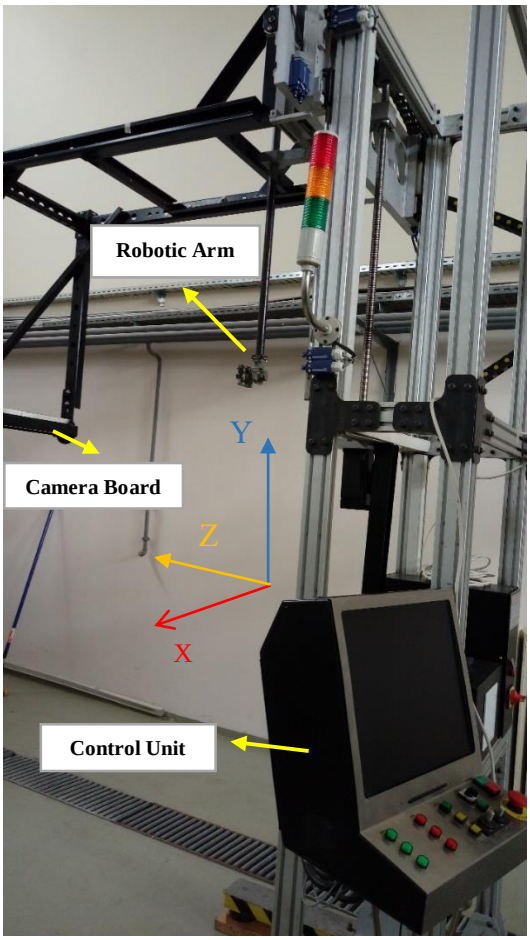

Figure 3.2. Robotic Arm

The model is a flat plate and in order to achieve equivalent values of the stiffness parameter with revolving wings experiments and according to the maximum possible

velocity of the robotic arm, the wing dimensions are scaled to have a chord length (*c*) of 92 mm, span length (*s*) of 184 mm and an aspect ratio of 2. The leading edge of the wings was formed by a carbon fiber pipe to provide spanwise rigidity. This leading edge carbon fiber pipe was extended at the wing root and it was clamped in an adapter which was connected to the robotic arm head. An overview of wing parameters is given in Table 3.1 and the wing models are shown in Figure 3.3.

Table 3.1. Wing size parameters

Property	Value
Chord (c)	92 mm
Span (s)	184 mm
Aspect ratio (AR)	2
LE carbon fiber pipe outer diameter	4 mm
LE carbon fiber pipe inner diameter	2 mm

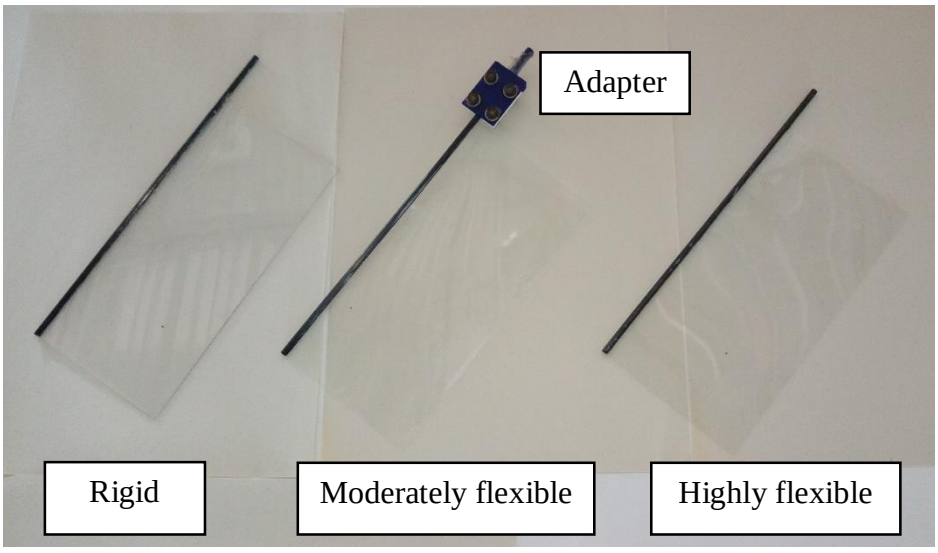

Figure 3.3. Wing models

3.2. Kinematics

The non-dimensional parameters to define motion kinematics are chord length traveled ($\delta^* = \delta/c$, where δ is the distance traveled by the wing) and convective time ($t^* = t \times V_t/c$, where t is the time and V_t is the terminal velocity). The translating wing motion starts from rest with 45 degrees of angle of attack and a constant acceleration to reach a predefined terminal velocity (V_t) of 0.08 m/s over a time interval corresponding to one chord length of travel (i.e. $0 < \delta^* < 1$). Subsequently, it continues to translate with the constant terminal velocity for three more chord lengths. Based on the chord length and the terminal velocity, the Reynolds number is 7360. An overview of wing kinematics is given in Table 3.2. The wing kinematics is illustrated in Figure 3.4.

Table 3.2. Wing kinematics

Property	Value
Constant acceleration phase	$0 < \delta^* < 1$
Constant velocity phase	$\delta^* > 1$
Chord length (c)	92 mm
Terminal velocity (V_t)	0.08 m/s
Reynolds number	7360
Acceleration	0.035 m/s^2
Angle of attack (α)	45 degrees

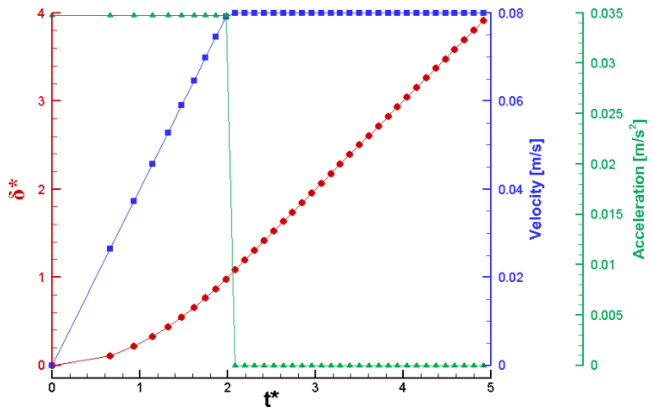

Figure 3.4. Wing kinematics

3.3. Wing Flexibility

Wing deformability can be measured by flexural stiffness (*EI*) which can be defined by two properties: Young's modulus of the wing material and the area moment of inertia. The resistance of the wing against the fluid-dynamic forces acting on the wing is called bending stiffness (Π_1) which shows the ratio of elastic bending forces to fluid dynamic forces acting on the wing (Equation 3.1) (Shyy et al., 2010):

$$\Pi_1 = \frac{Eh^3}{12(1-\upsilon^2)\rho V_t^2 c^3} \tag{3.1}$$

where E is the Young's modulus υ is the Poisson ratio, h is the thickness value, and V_t is the terminal velocity. In the bending stiffness parameter equation, a Poisson ratio (υ) of 0.4 for Plexiglas and PET is considered. 1000 (kg/m^3) is taken for the density of water. Three different models with different flexural stiffness have been considered in this study, having different materials and thicknesses. The wings properties are given in Table 3.3.

Table 3.3. Wing model properties

Description	Material	Young's modulus E [Nm^{-2}]	Thickness h [mm]	Flexural Stiffness (EI) [Nm^2]	Bending stiffness parameter Π_1
Rigid	Plexiglas	$\approx 3300 \cdot 10^6$	1	5.06×10^{-2}	65.5
Moderate flexibility	PET	$\approx 4350 \cdot 10^6$	0.175	3.57×10^{-4}	0.46
High flexibility	PET	$\approx 4500 \cdot 10^6$	0.125	1.34×10^{-4}	0.17

The wings have the same bending stiffness values with the revolving wings experiments. The terminal velocity in the revolving case was 0.2 m/s and the wings

had a chord length (c) 50 mm, which resulted in the Reynolds number of 10000. In the current study, the Reynolds number is 7360. The relative insensitivity of the flow structures to Reynolds number in this flow regime (Percin and van Oudheusden, 2015) allows for a proper comparison between the two tested motion kinematics.

3.4. Flow Field Measurements via Particle Image Velocimetry

Two dimensional – two component particle image velocimetry (2D2C-PIV) technique was employed to investigate the flow field around the surging-translating wings. Dantec FlowManager v4.60 commercial software was used to record the PIV images and DynamicStudio 2015a was used to process the PIV images. PIV system consists of different components and the corresponding procedures explained individually in the next sections.

3.4.1. Imaging and Field of View

Two 12-bit HiSense MkII CCD cameras were placed side-by-side in order to increase the field of view. The Hisense MKII camera has a sensor resolution of 1344 × 1024 pixel^2, and pixel size of 6.45 μm. Each camera was equipped with a Nikon 50 mm focal objective with numerical aperture of $f_{\#} = 2$. The right camera placed at a lower position in order to capture the flow around the wing trailing-edge properly. Both cameras were placed on the camera board that also translated with the wing model. Thus, the field of view is the same for all positions in the measurement. The images from both cameras were stitched according to the mapping information obtained from the calibration target image, yielding a final resolution of 2302 × 1338 pixel^2. The scale factor for both cameras is 16.67 (magnification factor = 0.059), which results in the field of view (FOV) of 247.5 mm × 143.9 mm. The calibration target and PIV cameras are shown in Figure 3.5. The schematic of the chordwise field of view with the rigid wing is depicted in Figure 3.6.

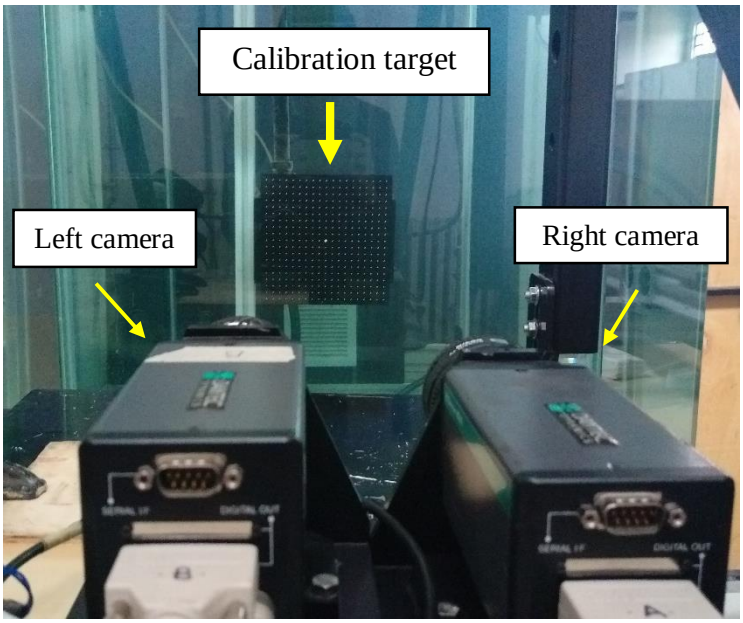

Figure 3.5. PIV cameras and the calibration target

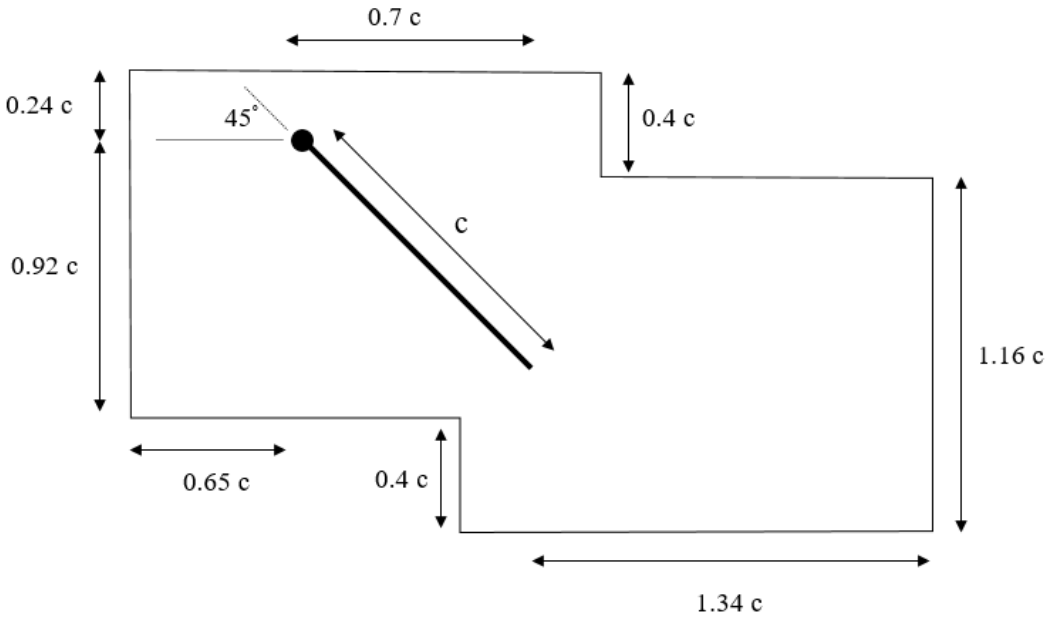

Figure 3.6. Schematic of field of view

3.4.2. Illumination

A double-pulsed Nd: YAG laser at a wavelength of 532 nm with a pulse energy of 120 mJ was used for illumination (Figure 3.7). Time interval between two consecutive laser pulses (time between two frames) is 9 ms. A Plano-Convex spherical lens with an effective focal length of 750 mm in addition to a Plano-Concave cylindrical lens with an effective focal length of -12.77 mm are used to generate a laser sheet at the 75% of span position. The spherical and cylindrical lenses are shown in Figure 3.8.

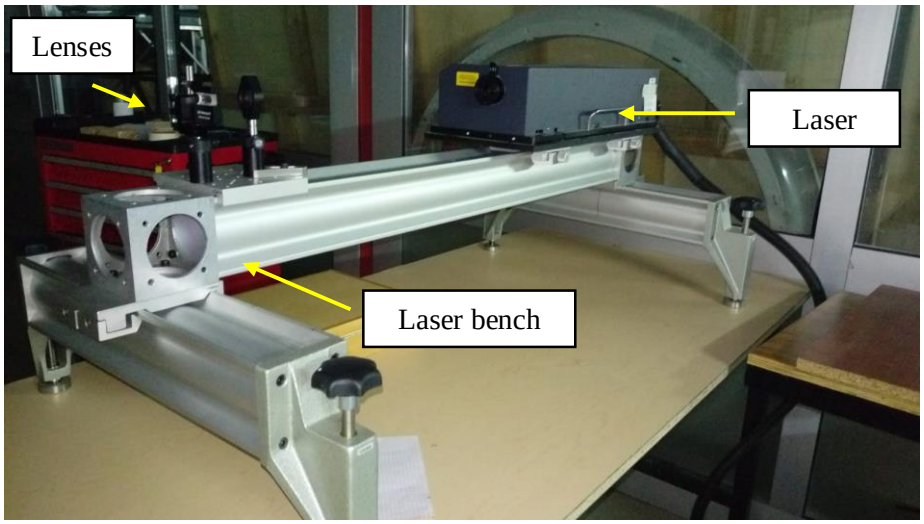

Figure 3.7. Laser and laser bench

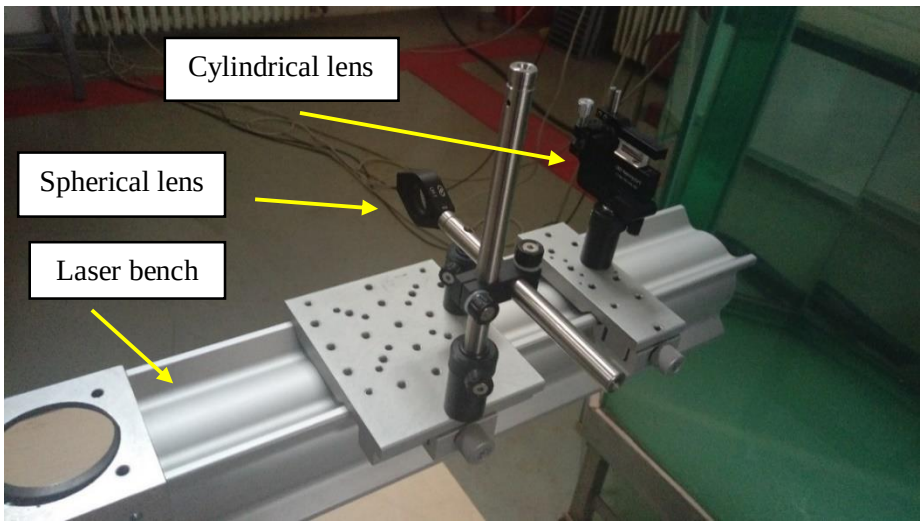

Figure 3.8. Spherical and cylindrical lenses

3.4.3. Seeding

Hollow glass spheres with a density of 0.21 gr/cm^3 and a mean diameter of 65 μm were used as tracer particles. They have good scattering properties and they can suspend in the water for a long time.

3.4.4. External Trigger

In order to capture images at a specific phase of motion, a magnetic sensor was used as an external trigger source. Seventeen magnets were placed on the robotic arm system with 0.25 chord length distance in between. When the sensor passes a magnet, it generates a TTL signal to trigger the image acquisition. Each magnet was checked before one set of experiment. The first magnet was placed at 0.032 δ^*, the second magnet at 0.25 δ^*, the third magnet at 0.5 δ^*, and this continues till the seventeenth magnet was placed at 4 δ^*. Figure 3.9 displays the magnets and the magnetic sensor.

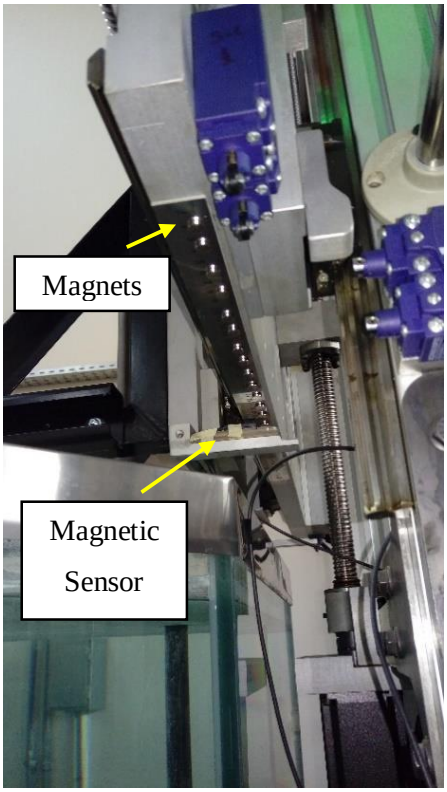

Figure 3.9. Magnetic sensor for external trigger.

3.4.5. Flow Condition

Since the laser was shot from the right side of cameras, the wings were selected to move from right to left such that the shadow of the carbon fiber leading edge fell on the pressure side of the wings. There was a pause of 1 minute after each set of experiment to let the water reach the quiescent condition before running the next experiment. The wings first went to the rest position of the measurement with the minimum speed in order not to disturb the flow. The PIV measurements done at the position (rest) showed that the upstream became quiescent after passing of 1 minute. A pause of 2 minutes at the rest position was given to the robotic arm to be on the safe side. The average time for each run was approximately 5 minutes.

3.4.6. Image Acquisition

In order to increase the signal to noise ratio of the velocity measurements, an ensemble averaging of 8 samples for each phase of the motion is used. For selecting the number of samples, the ensemble average of 1, 4, 8 and 16 samples were considered. The ensemble averaging of 8 samples were selected in calculations for two reasons. First, the difference between the LEV centroid position detected for the ensemble average of 8 and 16 samples was the same. Second, the out-of-plane vorticity contour converges after 8 number of samples (Figure 3.10).

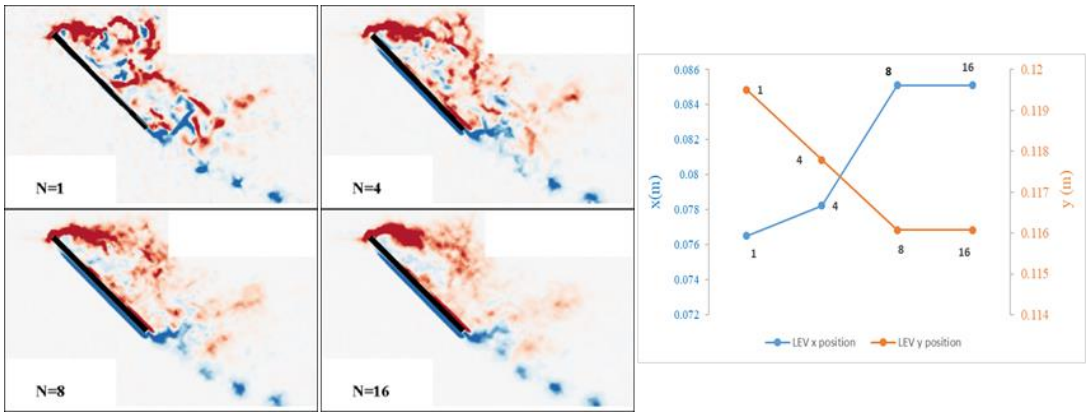

Figure 3.10. Left: The out-of-plane vorticity contours for different ensemble averaging samples. Right: LEV positions for different ensemble averaging samples

Image acquisition was done in three steps. First, the images corresponding to each position were exported separately. Second, the related images from right and left cameras for both frames were stitched, and in the final step, the resultant pair of images were imported to individual runs in DynamicStudio 2015a software for image processing. Experiments were repeated at least 20 times, and the 8 high quality images in term of having an adequate seeding density and minimum light reflections were selected for further processing.

Table 3.4 represents a summary of experimental settings for the PIV experiments. The experimental setup for the PIV measurements setup is shown in Figure 3.11.

Table 3.4. Summary of experimental settings for PIV

Camera	2 × 12 bit Hisense MK II CCD camera Sensor resolution: 1344 × 1024 pixel^2 2 × Nikon 50 mm camera lens, $f_{\#} = 2$ Pixel size: 6.45 μm
Imaging	Stitched image pixel size: 2302 × 1338 pixel^2 Field of view: 247.5 × 143.9 mm^2 Time between pulses (Δt): 9 ms Image magnification: 0.059 Scale factor: 16.67
Illumination and laser sheet	Nd: YAG laser, Solo 120XT Manufacturer: New wave research Maximum Energy: 120 mJ/pulse Wavelength: 532 nm Thickness: ≈ 4-5 mm Maximum repetition rate: 21 Hz
Optics	Spherical Lens: Plano-Convex, 750 mm FL Cylindrical Lens: Plano-Concave, -12.77 mm FL
Seeding	Glass bubbles 0.21 gr/cm^3 Mean diameter: 65 μm

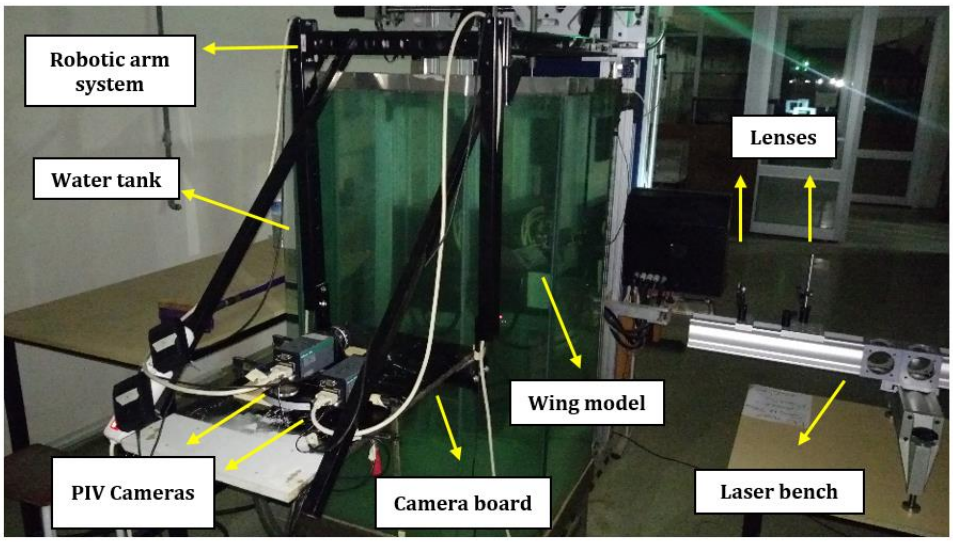

Figure 3.11. 2D-PIV setup

3.5. Experimental Setup for Revolving Wings (TU Delft)

The flow field around the wings were investigated by three tomographic measurement volumes combined to getter. The experimental setup, schematic top view of experimental setup, and wing kinematics are shown in Figure 3.12, 3.13 and 3.14, respectively.

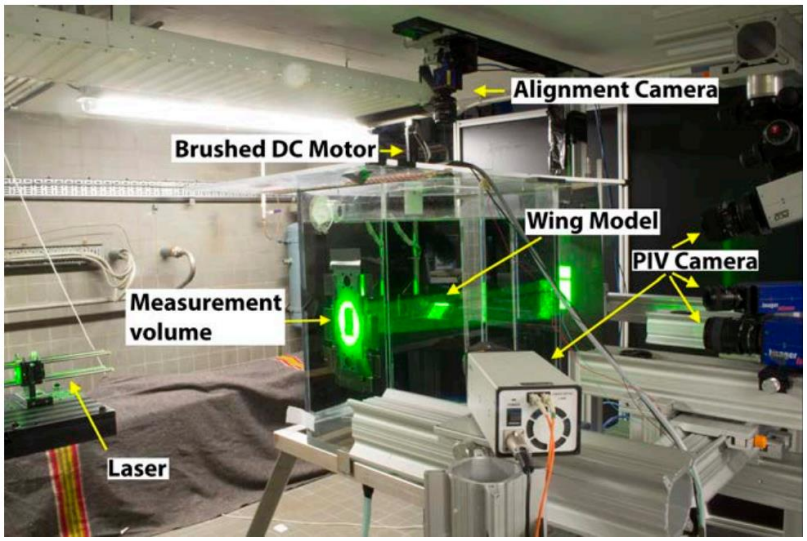

Figure 3.12. Tomographic PIV setup for revolving wings (van de Meerendonk, 2016)

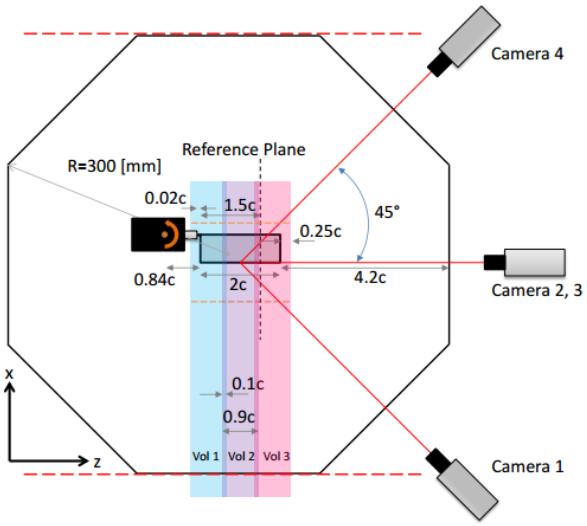

Figure 3.13. Schematic top view of experimental setup in revolving wing experiments (van de Meerendonk, 2016)

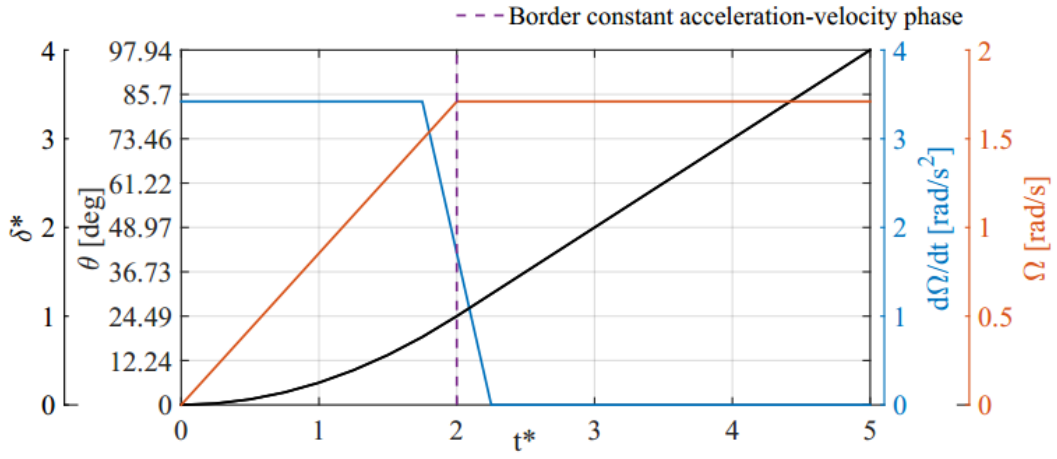

Figure 3.14. Motion kinematics for revolving wings (van de Meerendonk, 2016)

3.6. Data Processing

In this section, the calibration, image pre-processing methods, and velocity vector calculations are explained. DynamicStudio 2015a software from DantecDynamics is used for data processing.

3.6.1. Calibration

Two images from the two cameras were stitched and imported to DynamicStudio 2015a. The stitched calibration image is shown in Figure 3.15. According to the calibration target, the scale factor was calculated as 16.67 (Magnification factor = 1/16.67=0.059). The calibration procedure was done in 4 steps. In the first step, the plane of interest was characterized and the laser sheet position was determined. In the next step, the calibration target was inserted to the water tank and fixed in a way to remain in a vertical position. In the third step, the cameras were focused to the calibration target, and a single image acquired from both cameras. In the final step, the scale factor was calculated according to the distance between the white dots on the target and pixel values.

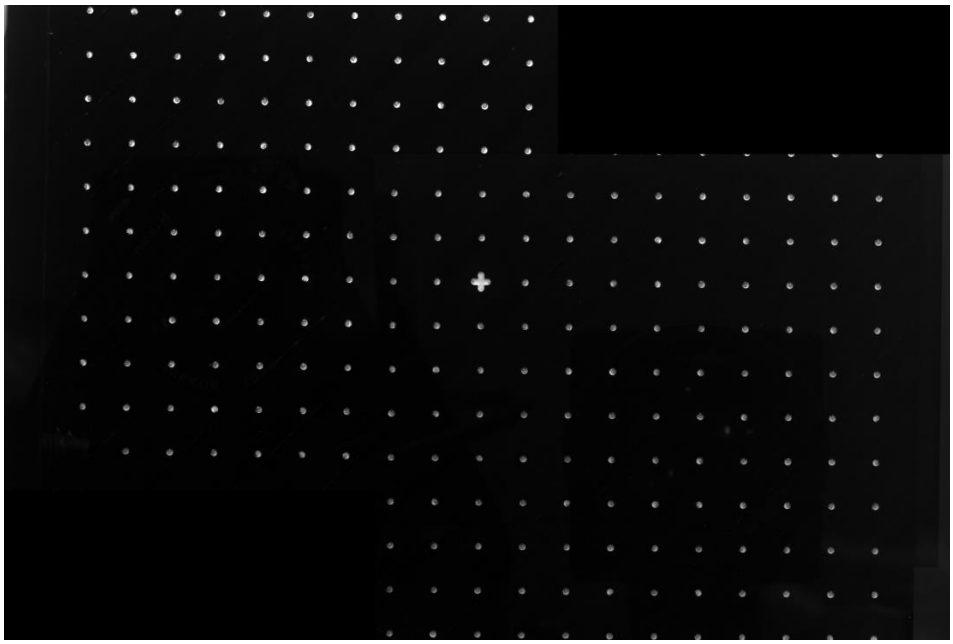

Figure 3.15. Stitched calibration image

3.6.2. Image Pre-processing

All images were pre-processed in 6 steps to enhance the quality of images, and a sample for each step is illustrated in the following section. An example of raw image

is shown in Figure 3.16-A. In the first step, a mask was defined around the wings (Figure 3.16-B), and in the second step, the images were masked by the corresponding defined mask (Figure3.16-C). In order to reduce the background noise and remove the reflections, the mean minimum pixel values were calculated (Figure 3.16-D), and subtracted from the masked images (Figure 3.16-E). CCD leakage was detected in the images, and to reduce its effect, image balancing was performed on the images. In the fifth step, the image balance, a light sheet balance map with 15×15 smooth cell size was generated, and in the last step, the light sheet balance map applied to images (Figure 3.16-F).

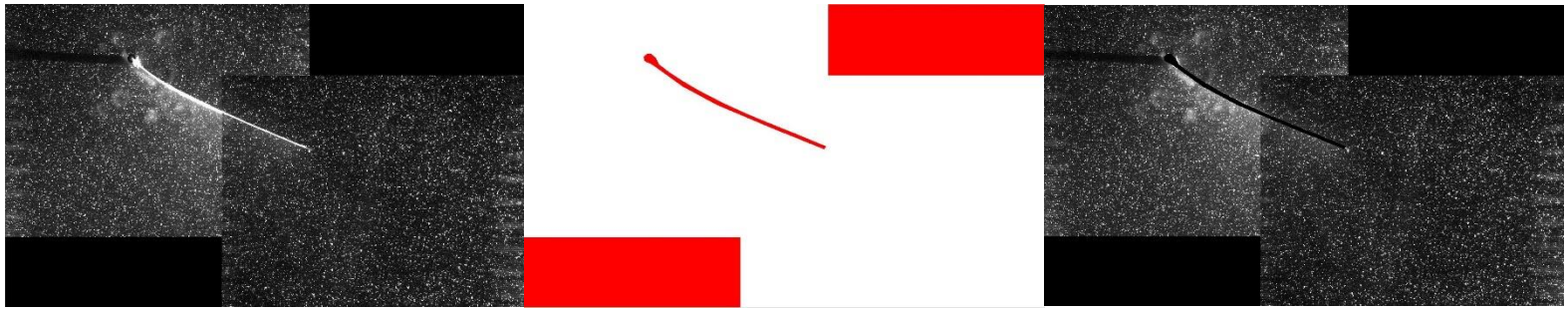

(A) A sample of stitched raw image (B) A sample of defined mask (C) Masked image

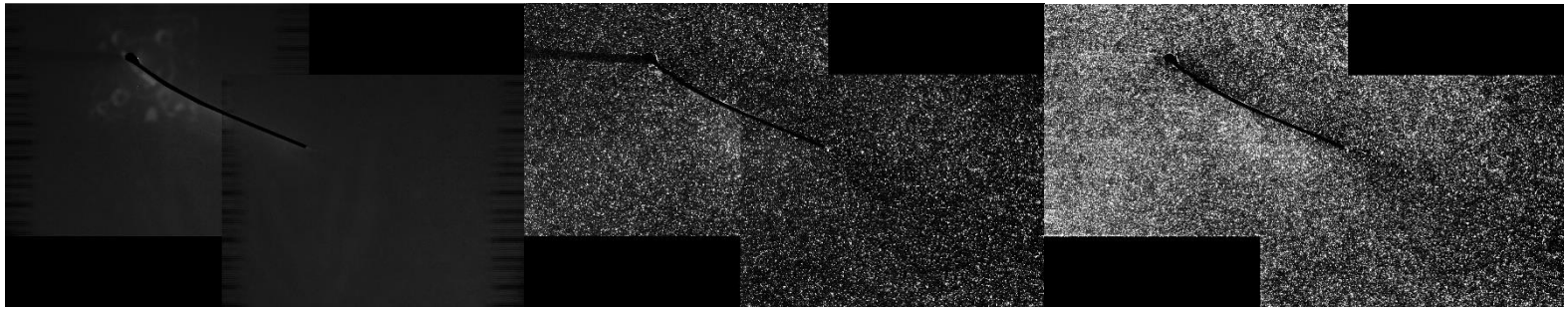

(D) Mean minimum pixel values (E) Subtracted imaged from background noise (F) Balanced image

Figure 3.16. Image pre-processing steps

3.6.3. Vector Calculations (Processing)

For calculation of velocity vectors, Image processing was done in 4 steps. A sample is shown for each step in the following section. In the first step, the balanced images were cross-correlated with an interrogation area size of 64 × 64 pixels^2 with 75% overlap, which resulted in an 1.72 mm vector spacing and a spatial resolution of 53 vectors/c (Figure 3.17-A). In the second step, the velocity vectors were masked with the corresponding mask defined in the pre-processing section (Figure 3.17-B). In the next step, the universal outlier detection technique was applied to the cross-correlation results to detect and substitute the unreliable velocity vectors (Figure 3.17-C) (Westerweel and Scarano, 2005). In the final step, ensemble averaging of 8 samples were calculated for each phase of the motion (Figure 3.17-D).

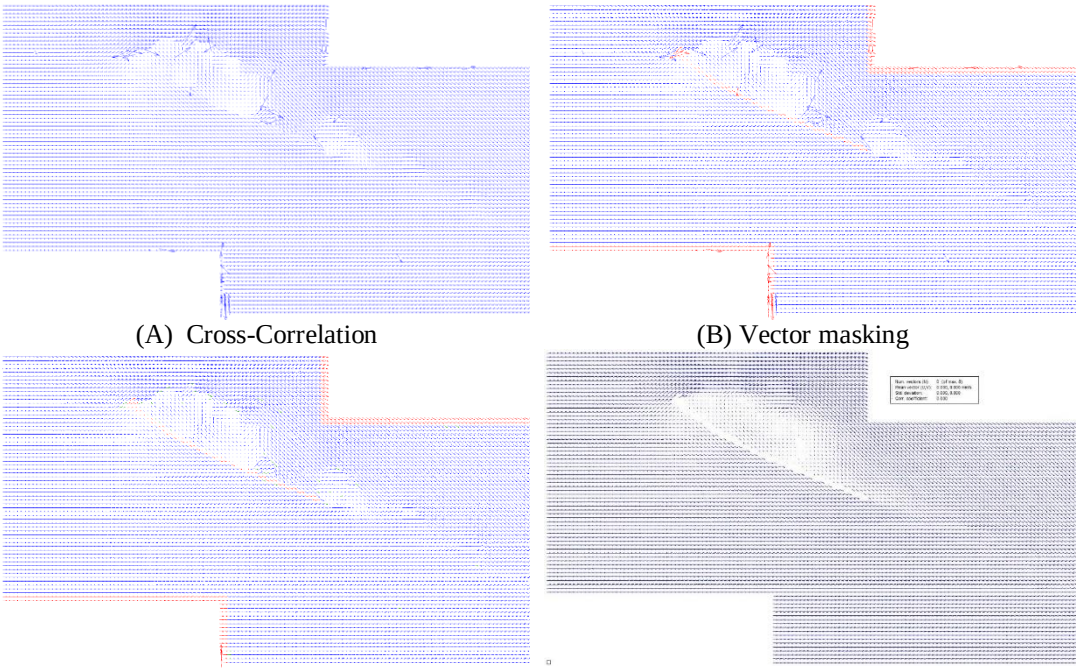

(A) Cross-Correlation (B) Vector masking

(C) Universal outlier detection (D) Ensemble averaging

Figure 3.17. Vector calculation steps

3.7. LEV Centroid Detection Method

There are a number of different methods used for the detection of vortex center such as vorticity magnitude, normalized helicity, Q criterion and γ_1 integral method. In this study, the γ_1 and γ_2 functions are used to detect the LEV centroid and core, respectively.

γ_1 method (Graftieaux et al., 2001**):** One method for vortex detection is the calculation of γ_1 integral. γ_1 is a non-Galilean invariant scalar function which measures the relative rotation around all grid points over a definable interrogation window at which it detects the vortex core as the point where the velocity vectors around a point have a normal distance to the point. In other words, if a radius vector is drawn from a point to the velocity vectors around the point, that grid point can be the vortex core if the angle between these two vectors become approximately 90 degrees. The equation 3.2 defines the γ_1 function.

$$\gamma_1(\mathrm{P}) = \frac{1}{N}\sum_{M}\frac{(\mathbf{L}_{PM}\times\mathbf{U}_M)\ .\ \mathbf{z}}{\|\mathbf{L}_{PM}\|.\|\mathbf{U}_M\|} = \frac{1}{N}\sum_{M}\sin\theta_M \qquad (3.2)$$

where N is the number of grid points M inside the definable area surrounding P and M and $\mathbf{z}$ is the unit normal vector to the measurement plane. $\mathbf{U}_M$ is the velocity vector, $\mathbf{L}_{PM}$ is the radius vector from the grid points to the velocity vectors and θ_M is the angle between radius vector and the velocity vector. Equation 3.2 is the cross product of the velocity vector and radius vector over the multiplication of their magnitudes, which results the $\sin\theta_M$. The γ_1 has the values from 0 to 1, and the vortex core is the point where γ_1 has the highest value $\|\gamma_1\|$.

γ_2 function (Graftieaux et al., 2001)**:** The vortex boundary can be identified by calculation of γ_2 function. γ_2 function has the same algorithm as γ_1 function; however, the local convection velocity plays a role in the algorithm and γ_2 function can be defined as equation 3.3:

$$\gamma_2(\mathrm{P}) = \frac{1}{N}\sum_{M} \frac{\left(\mathbf{L}_{PM}\times(\mathbf{U}_M-\mathbf{U}_p)\right)\,.\,\mathbf{z}}{\|\mathbf{L}_{PM}\|.\left\|\mathbf{U}_M-\mathbf{U}_p\right\|} \tag{3.3}$$

where $\mathbf{U}_p$ is the local convection velocity. $\gamma_2(\mathrm{p})$ is a Galilean invariant scalar function. A vortex core is represented by regions of $\|\gamma_2\| > 2/\pi$ which the flow is locally dominated by the rotation.

3.8. Circulation

The circulation (vorticity flux) can be calculated as follows (Equation 3.4):

$$\Gamma = \oint \omega_z dxdy\,;\ \Gamma^* = \frac{\Gamma}{c\,V_{terminal}} \tag{3.4}$$

The integration is over the chordwise oriented integration plane. The region that $\gamma_2 > 2/\pi$ is defined as the LEV circulation region in the calculations.

3.9. Analysis of the Measurement Errors

3.9.1. Accuracy of Robotic Arm

As mentioned above, the motion kinematics consist of a constant acceleration phase and a constant velocity phase. The percent error of displacement at different phase of the motion is given in Figure 3.18. In the constant velocity phase, the robotic arm has an approximately accurate displacement (maximum error of 0.13%). For eight samples, the displacement-time graph of the motion is derived from oscilloscope in the control unit and all graphs are identical which means that in all samples, the wings were moved with the same kinematics.

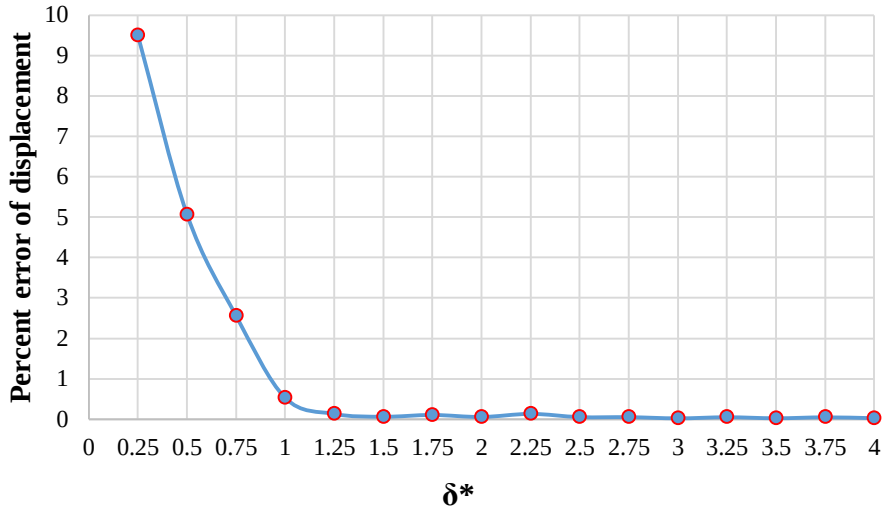

Figure 3.18. Percent error of robotic arm displacement at different phases of motion

3.9.2. Uncertainty in Velocity Vectors

PIV technique finds velocity vectors by dividing the particle displacement between two consecutive frames by the time interval between the frames. Different parameters affect the determination of the particle displacements such as particle image size, level of noise, velocity gradients, and interrogation window size which also affect the uncertainty. The general uncertainty reported in the literature for displacement in pixels is between 0.05-0.1 pixel (Brossard et al., 2015). In the current study, we selected 0.1 pixel for calculation of uncertainty. The calculation is as follows:

$$\varepsilon_U = \sqrt{\left(\frac{\partial U}{\partial \Delta t}\varepsilon_{\Delta t}\right)^2 + \left(\frac{\partial U}{\partial \Delta x}\varepsilon_{\Delta x}\right)^2} = \sqrt{\left(\frac{-\Delta x}{\Delta t^2}\varepsilon_{\Delta t}\right)^2 + \left(\frac{1}{\Delta t}\varepsilon_{\Delta x}\right)^2} = \frac{1}{\Delta t}\sqrt{(U\varepsilon_{\Delta t})^2 + (\varepsilon_{\Delta x})^2} =$$

$$\frac{\varepsilon_{\Delta x}}{\Delta t} = \frac{0.1}{9\times10^{-3}} = 11.11 \text{ pixel/sec}$$

$$\varepsilon_U = \frac{11.11 \text{ pixel/sec}}{16.67 \text{ pixel/mm}} = 0.66 \frac{\text{mm}}{\text{sec}} = 6.66\times10^{-4} \text{ m/s} \quad (3.5)$$

The uncertainty of terminal velocity is $\frac{6.66\times10^{-4}}{0.08} \times 100 = 0.83\%$

3.9.3. Uncertainty in the LEV Circulation

For calculation of uncertainty in the LEV circulation, first, the LEV circulation for each sample for a phase of the motion is calculated. Then the standard deviation of eight samples is computed. The calculation is as follows:

$$\text{Measured standard deviation, } \sigma = \left[\frac{1}{N}\sum_{i=1}^{N}(\Gamma_i - \bar{\Gamma})^2\right]^{1/2} = 0.07712774 \quad (3.6)$$

$\text{Uncertainty} = \frac{k\,\sigma}{\sqrt{N}}$ where k is the coverage factor and N is the number of samples. For 95% confidence level, the k is 1.96, therefore:

$$\text{Uncertainty} = \frac{1.96 \times 0.07712774}{\sqrt{8}} = 0.053446797 \text{ m}^2/\text{s}$$

$$\text{Percent uncertainty of the reported LEV circulation, } \frac{0.053446797}{1.098538493} \times 100 = 4.86\%$$

3.9.4. Uncertainty in the LEV Centroid

The uncertainty calculation of LEV centroid is done for x and y position, separately. The procedure is the same as uncertainty calculation of LEV circulation.

Uncertainty calculation in x:

$$\text{Measured standard deviation, } \sigma = \left[\frac{1}{N}\sum_{i=1}^{N}(x_i - \bar{x})^2\right]^{1/2} = 0.001594802 \quad (3.7)$$

$$\text{Uncertainty} = \frac{k\,\sigma}{\sqrt{N}} = \frac{1.96 \times 0.001594802}{\sqrt{8}} = 0.001105141 \text{ m}$$

$$\text{Percent uncertainty of the reported LEV x position, } \frac{0.001105141}{0.090264299} \times 100 = 1.22\%$$

Uncertainty calculation in y:

$$\text{Measured standard deviation, } \sigma = \left[\frac{1}{N}\sum_{i=1}^{N}(y_i - \bar{y})^2\right]^{1/2} = 0.001426434 \quad (3.8)$$

$$\text{Uncertainty} = \frac{k\,\sigma}{\sqrt{N}} = \frac{1.96 \times 0.001426434}{\sqrt{8}} = 0.000988468 \text{ m}$$

Percent uncertainty of the reported LEV y position, $\frac{0.000988468}{0.114349115} \times 100 = 0.86\%$

The summary of uncertainty values is given in Table 3.5.

Table 3.5. Summary of uncertainty values

	Velocity (/ V_t%)	LEV Circulation (/ $\bar{\Gamma}$%)	LEV x position (/ $\bar{x}$%)	LEV y position (/ $\bar{y}$%)
Uncertainty	6.66×10^{-4} m/s (0.83%)	0.053446797 m^2/s (4.86%)	1.10514 mm (1.22%)	0.988468 mm (0.86%)

CHAPTER 4

RESULTS AND DISCUSSION

In this chapter, the results of the study are discussed in three sections. In the first section, the geometric angle of attack for different wings are presented. In the second section, the flow structures and characteristics for translating flexible wings are discussed. In the third section, the LEV characteristics including the LEV circulation, comparison between LEV circulation and TEVs circulation, and LEV position are presented.

4.1. Geometric Angle of Attack

The angle of attack of the wing model was set as 45 degrees at the leading edge by the control unit of the robotic arm. When the wings start to move, the rigid wing has a constant angle of attack during the motion, whereas the flexible wings deform during the translation which results in changing of angle of attack. The geometric angle of attack can be defined as the angle between the wing motion direction and the line connecting the leading edge and trailing-edge (Equation 5.1). Figure 4.1 depicts the schematic net force acting on the wing and geometric angle of attack for rigid and flexible wings according to the study of van de Meerendonk (2016).

$$\alpha_{geo} = \tan^{-1}\left(\frac{Y_{LE} - Y_{TE}}{X_{LE} - X_{TE}}\right) \tag{4.1}$$

where Y_{LE} is the leading edge vertical position, Y_{TE} is the trailing-edge vertical position, X_{LE} is the leading edge horizontal position, and X_{TE} is the trailing-edge horizontal position.

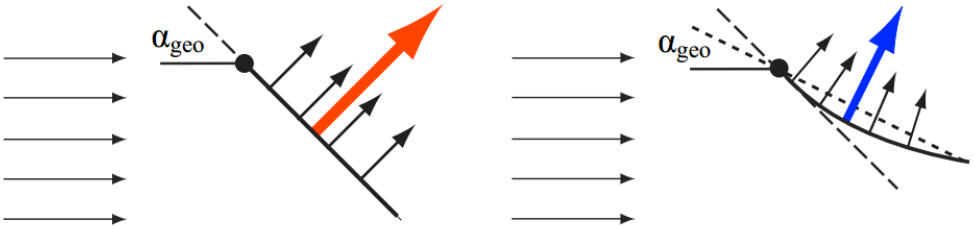

Figure 4.1. Schematic of net force acting on the wing and geometric angle of attack. Left: Rigid wing. Right: Flexible wing. Small vectors show the local net forces along the chord and the big vectors represent the resultant net force (van de Meerendonk, 2016)

It is put forward by van de Meerendonk (2016) that the resultant force direction for the revolving flexible wings is normal to the line connecting leading edge to the trailing edge in the deformed state as shown in Figure 4.1. This is basically due to the dominance of the pressure forces which are generated due to the low-pressure region formed by the leading edge vortex. For calculation of geometric angle of attack, first the x and y position of the leading edge and trailing edge in pixel values from PIV images were selected and then the geometric angle of attack according the selected points were calculated. It was shown by van de Meerendonk (2016) that there was a linear twist in revolving wings, thus weighted average of root and tip geometrical angle of attack in revolving wings with respect to 75% of span position was calculated for proper comparison with that of the translating wings. The temporal evolution of geometric angle of attack for translating flexible wings at 75% of span position, and weighted average of tip and root geometric angle of attack in revolving flexible wings are shown in Figure 4.2. It is clear that the highly flexible wing deforms more than the moderately flexible one and presumably the force vector is tilted more towards the lift direction due to relatively lower geometric angle of attack (see Figure 4.1). In the moderately flexible wing, the geometric angle of attack changes after acceleration phase (δ^*=1), and at the end of the constant velocity phase (δ^*=4), it reaches to the same value in starting position of constant velocity phase. In the highly flexible wing, the geometric angle of attack continues to decrease after acceleration phase.

The comparison between the geometric angle of attack in both cases reveals that the geometric angle of attack in translating flexible wings is smaller than that of the revolving flexible wings. The reason for this difference may be due to the wing twist in revolving wings in which the wing root avoids and restricts the wing deformation in spanwise direction. In the revolving wings, the wing tip deforms more than the wing root due to the wing twist. The average difference of geometric angle of attack between two motion kinematics in moderately flexible and highly flexible wings during constant velocity phase are 1.5 and 2.4 degrees, respectively.

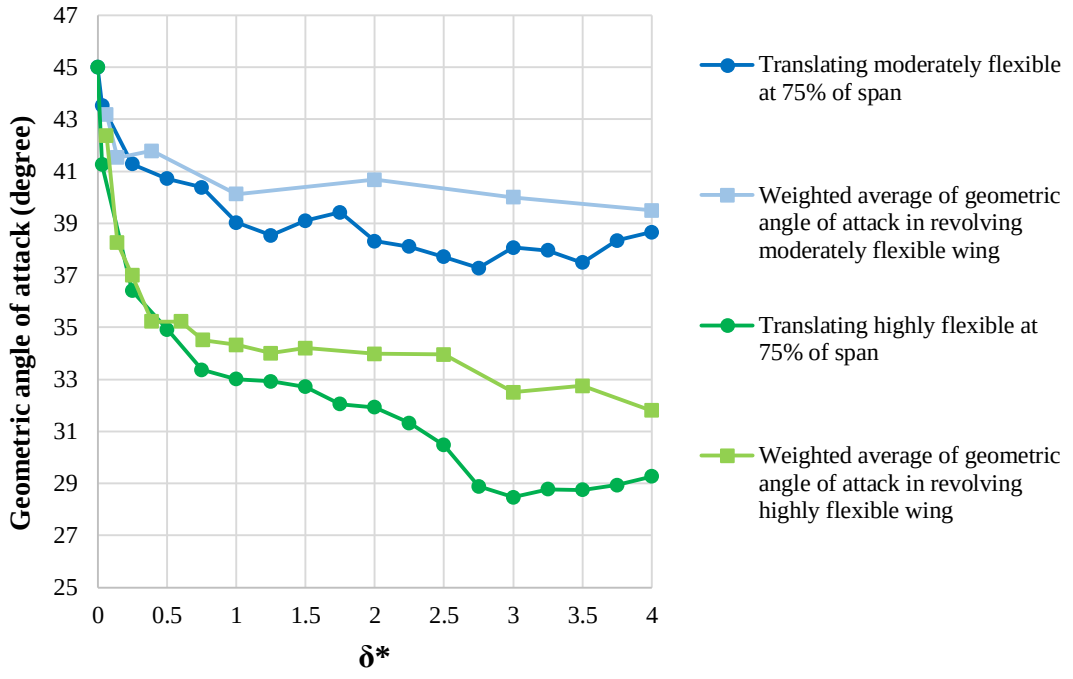

Figure 4.2. Temporal evolution of geometric angle of attack for translating flexible wings and weighted average of tip and root geometric angle of attack for revolving flexible wings

4.2. Flow Characteristics

The out-of-plane vorticity contours at the 75% span position for the rigid wing at different chord lengths of travel are shown in Figure 4.1. In the accelerating phase of the motion, coherent vortical structures can be seen at the leading edge and trailing

edge of the rigid wing. At the end of accelerating phase, the LEV starts to burst and after passing one chord length with a constant velocity at δ^*=2, the LEV bursts to smaller clusters of vortical structures and lifts off from the wing upper surface. At δ^*=2 to δ^*=2.75, a coherent train of TEVs can be observed extending into the wake. At δ^*=3, the shear layers emanating from the leading and trailing edges interact, and this interaction leads to small-scale vorticity pockets populating the wake. After three chords traveled, the flow is completely detached from the wing surface. Less coherent vortex formation and a chaotic flow field with an elongated incoherent positive vorticity layers emanating from the leading edge after δ^*=2 can be observed from vorticity contours. After δ^*=3.5, the TEVs cannot maintain their coherency resulting in the accumulation of counter-rotating vortical structures ending in fully chaotic flow.

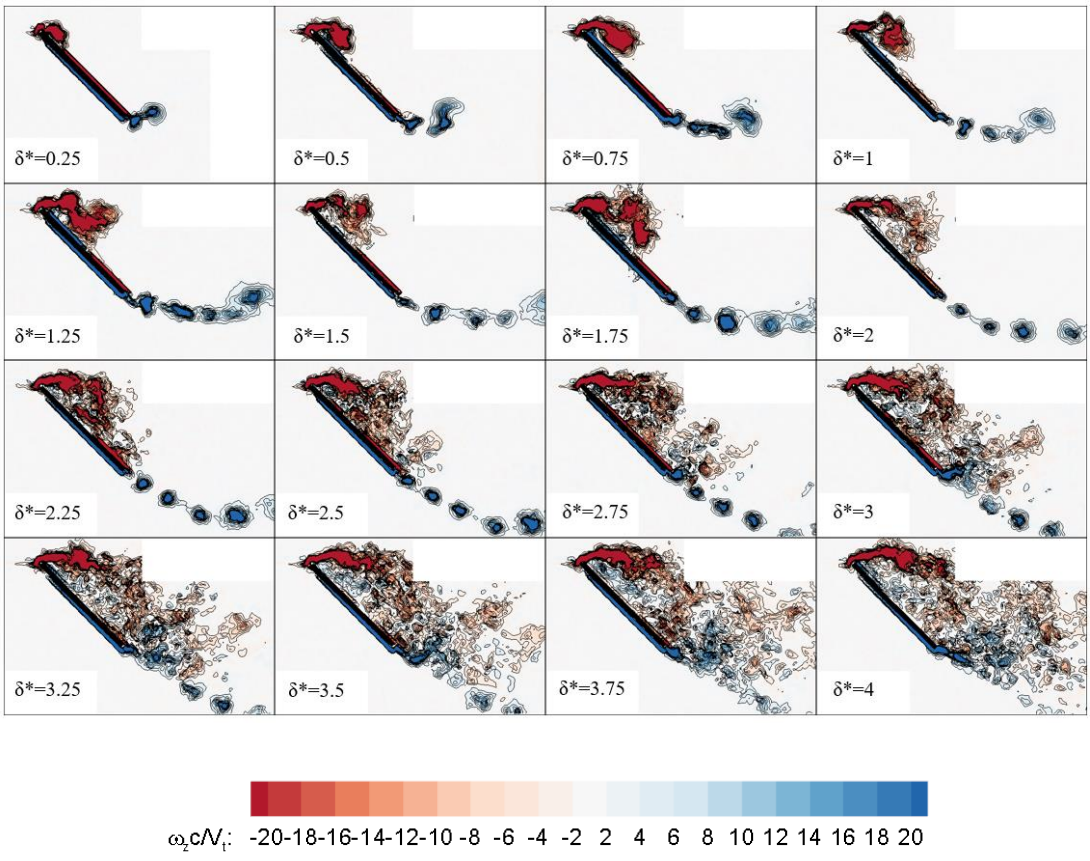

Figure 4.3. The out-of-plane vorticity contours of the rigid wing at the 75% span position for different chord lengths of travel

Velocity magnitude contours and streamlines for the rigid wing at different phases of motion are given in Figure 4.4. In the initial phases of the motion (i.e., $\delta^* < 2$), the attached LEV can be seen; however, after $\delta^*=2$, flow tends to lift off from the wing surface. The first LEV burst and sheds to the wake and subsequently, a secondary LEV is generated. The detached flow reattaches partially, and secondary LEV also lifts off from the wing surface. Some streamlines show reattachment after $\delta^*=3$, which cannot be reliable completely, due to the interpolation of Tecplot software in which some streamlines passed through the wing surface. The flow over upper surface of the wing at initial phases to a greater or lesser extent horizontal, whereas in the constant velocity phase, the flow tilted downward interacting with the flow passing from wing lower surface. The meeting location of flow passing from upper and lower surfaces of the wing can be seen at final phases of motion.

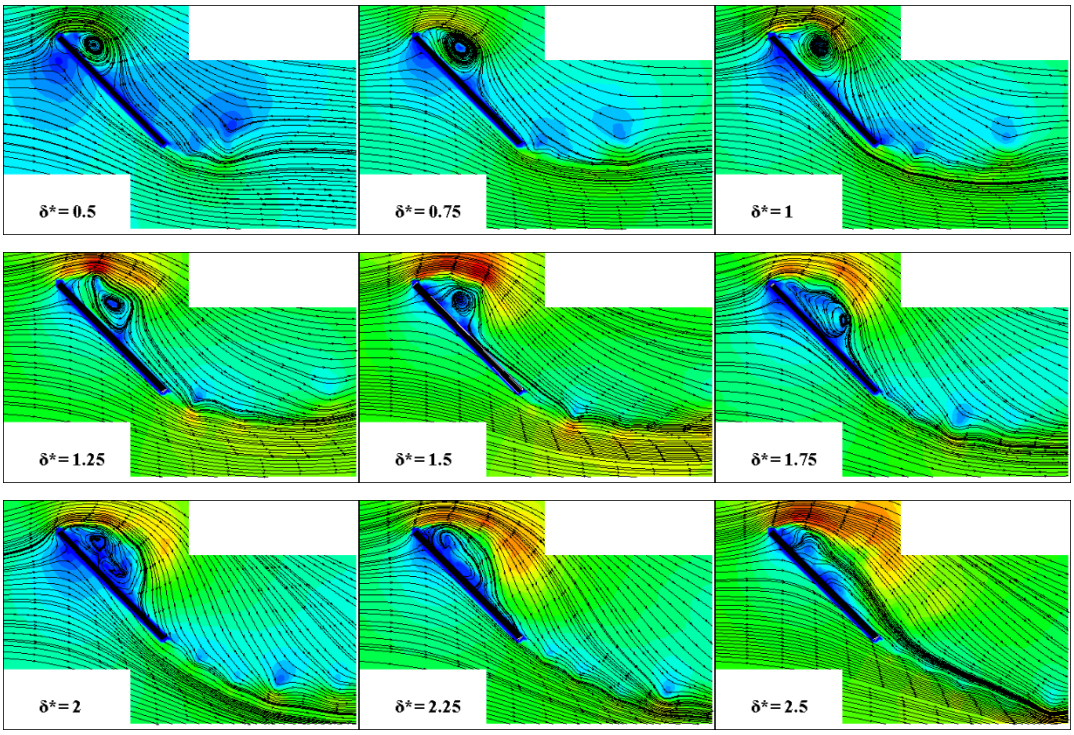

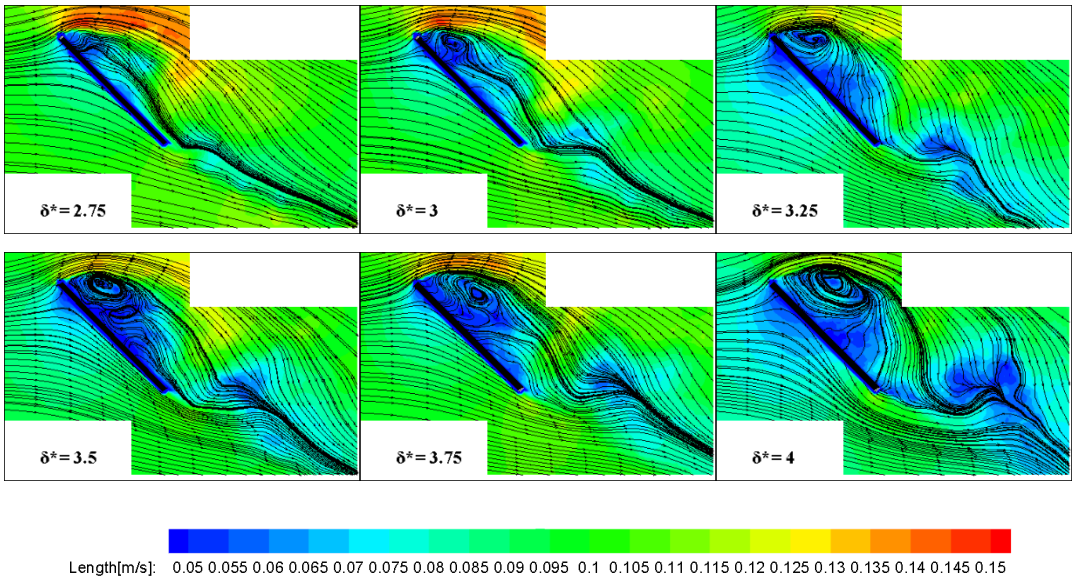

Figure 4.4. Velocity magnitude contours and streamlines for the rigid wing

The out-of-plane vorticity contours at the 75% span position for different chord length traveled by the wings are shown in Figure 4.5. The out-of-plane vorticity contours show similar behavior and vortex formations: a coherent LEV and a train of trailing edge vortices at the acceleration phase for rigid and flexible wings. At the end of acceleration phase, a lifted off fragmented LEV is present in the flow fields, which is in accordance with those reported in the literature (Percin and van Oudheusden, 2015). In the subsequent stages, the flow tends to be detached from the wing surface in rigid and moderately flexible wings. In highly flexible wings, the flow stays attached to the wing surface completely, due to the deflection of the wing and thus smaller geometric angle of attack. The LEV in the highly flexible wing stays closer to the wing surface.

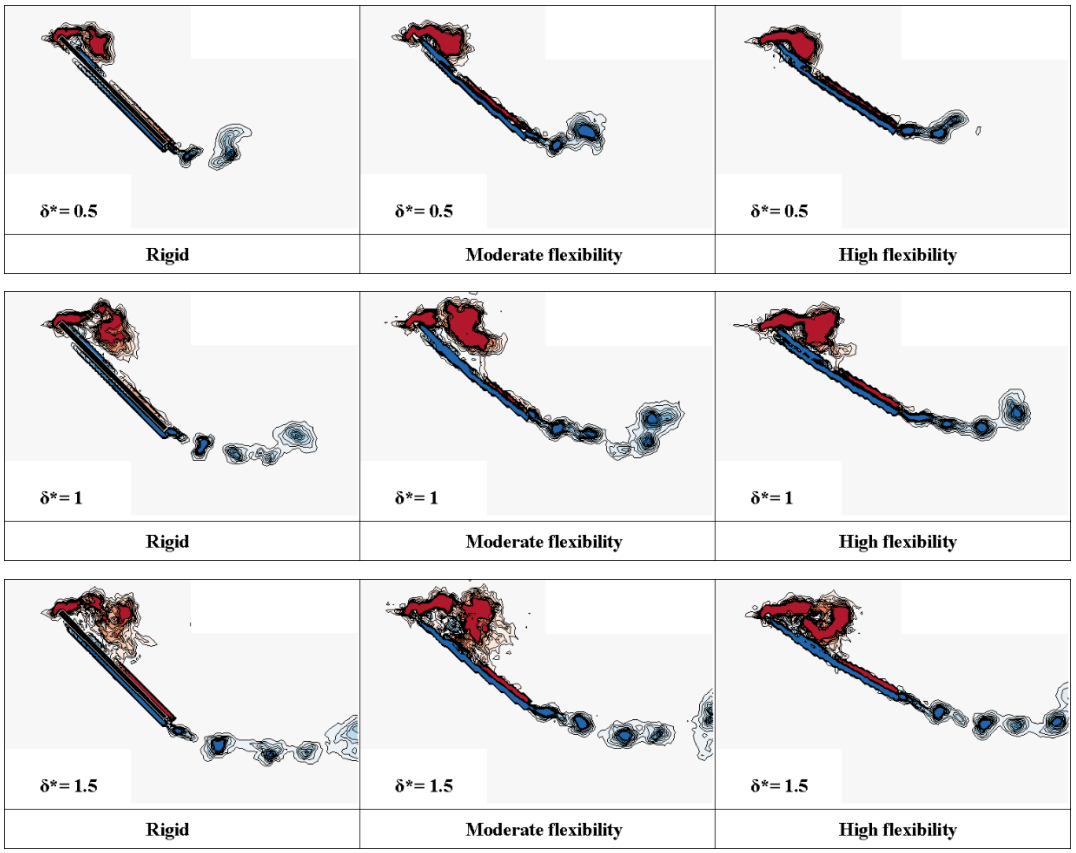
δ*= 0.5
δ*= 0.5
δ*= 0.5
Rigid
Moderate flexibility
High flexibility
δ*= 1
δ*= 1
δ*= 1
Rigid
Moderate flexibility
High flexibility
δ*= 1.5
δ*= 1.5
δ*= 1.5
Rigid
Moderate flexibility
High flexibility
δ*= 2
δ*= 2
δ*= 2
Rigid
Moderate flexibility
High flexibility
δ*= 2.5
δ*= 2.5
δ*= 2.5
Rigid
Moderate flexibility
High flexibility

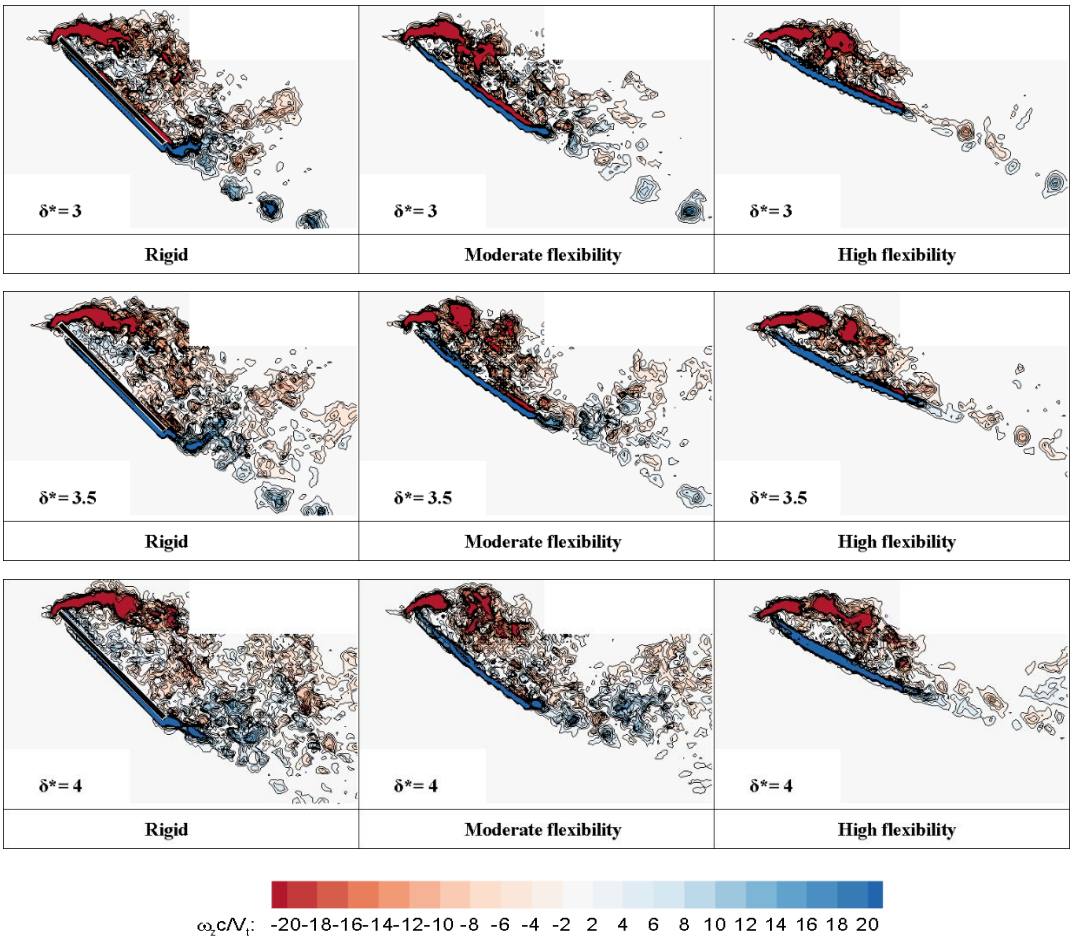

Figure 4.5. The out-of-plane vorticity contours at the 75% span position for different chord lengths of travel

The velocity magnitude contours and streamlines for three wings at δ^*=1, 2, 3 and 4 are depicted in Figure 4.6.

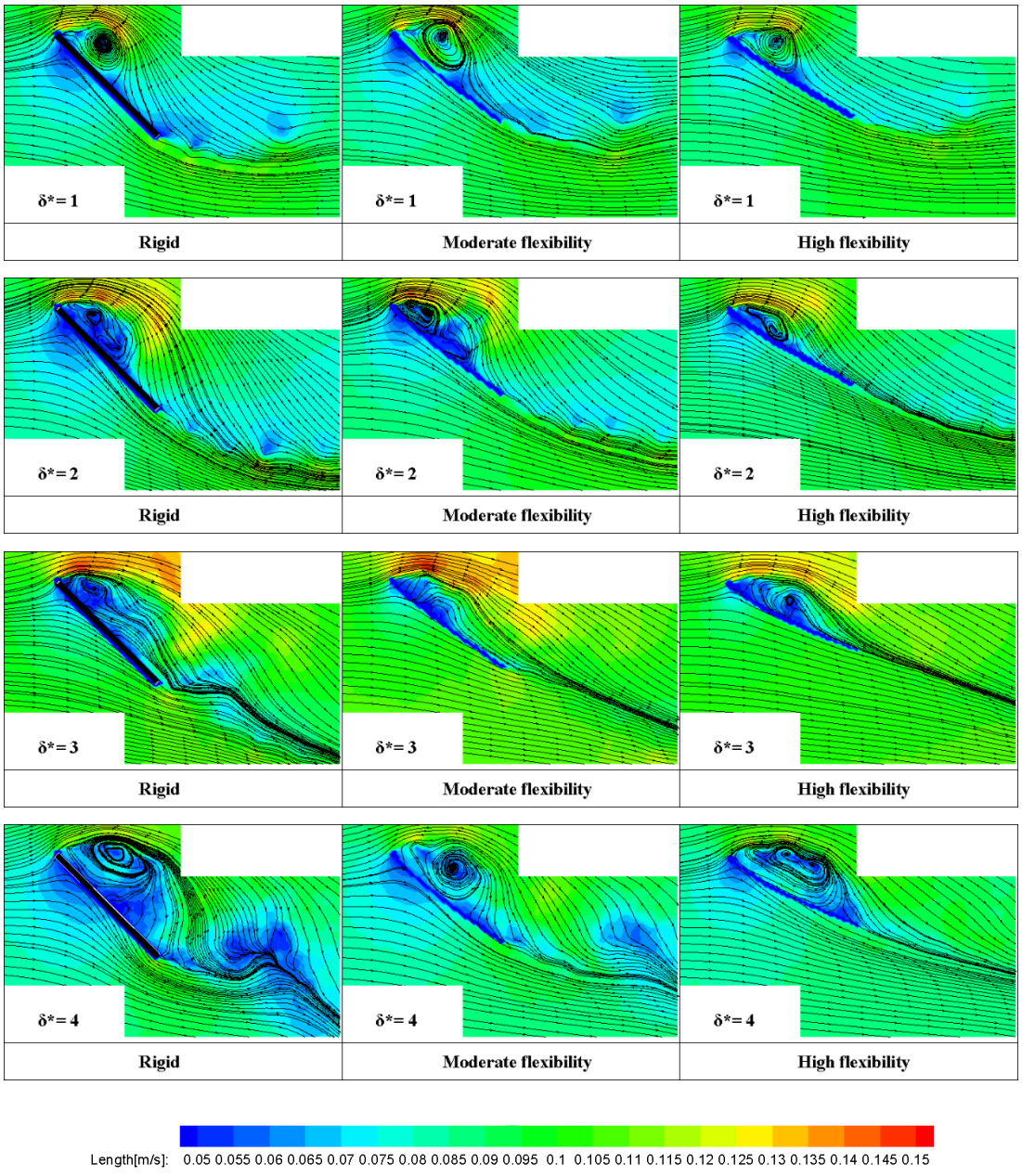

Figure 4.6. Velocity magnitude contours and streamlines for three wings at δ^*=1, 2, 3, and 4

The flexible wings show an attached flow throughout the motion, specifically in highly flexible wing in which the flow leaves the trailing-edge tangentially. Due to the deflection of the wing and thus, smaller geometric angle of attack, the LEVs and flow stays closer to the wing. In flexible wings, the flow from upper and lower surfaces

meet each other smoothly, while in the rigid wing, the flow passing from lower surface rises and makes more chaotic flow in wake region of the wing.

4.2.1. Comparison of Flow between Revolving and Translating Wings

Since the flow in the revolving motion was from right to left, the vorticity contours in the translating motion case are mirrored with respect to the y-axis, and the contour levels are changed to have the same level as the revolving case. The out-of-plane vorticity contours for δ^*=1.0, 1.5, 2, and 4 with respect to the 75% span position are shown in Figures 4.7, 4.8, 4.9 and 4.10, respectively.

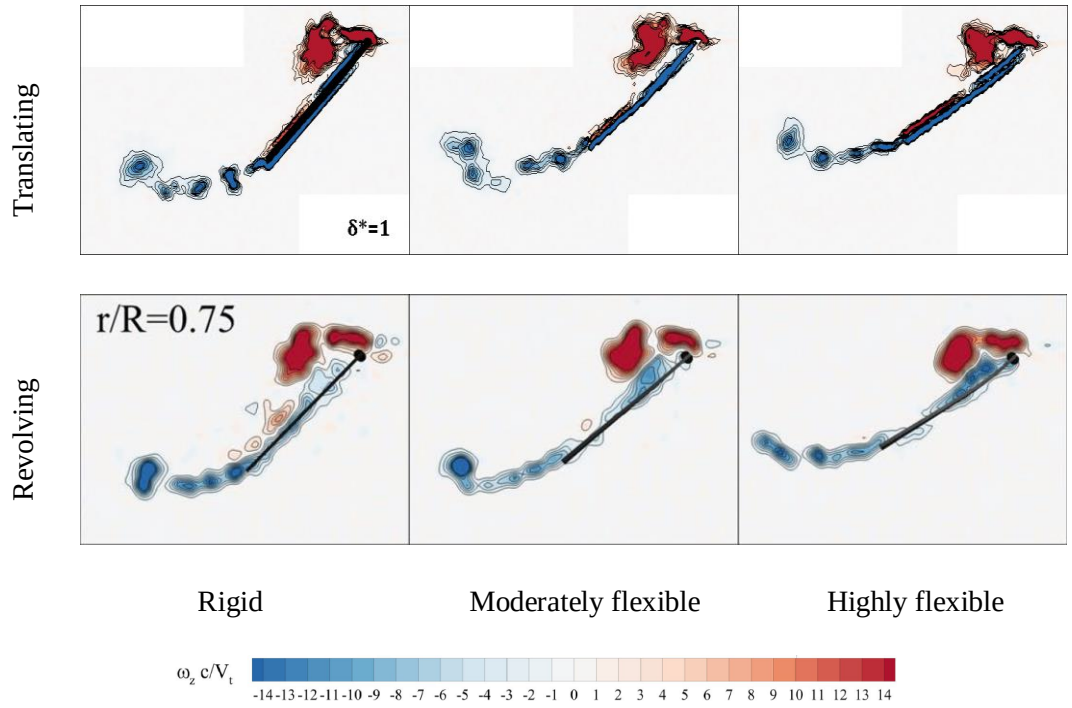

Figure 4.7. The out-of-plane vorticity contours for δ^*=1.0 with respect to the 75% span position. Top: Translating wings. Bottom: Revolving wings

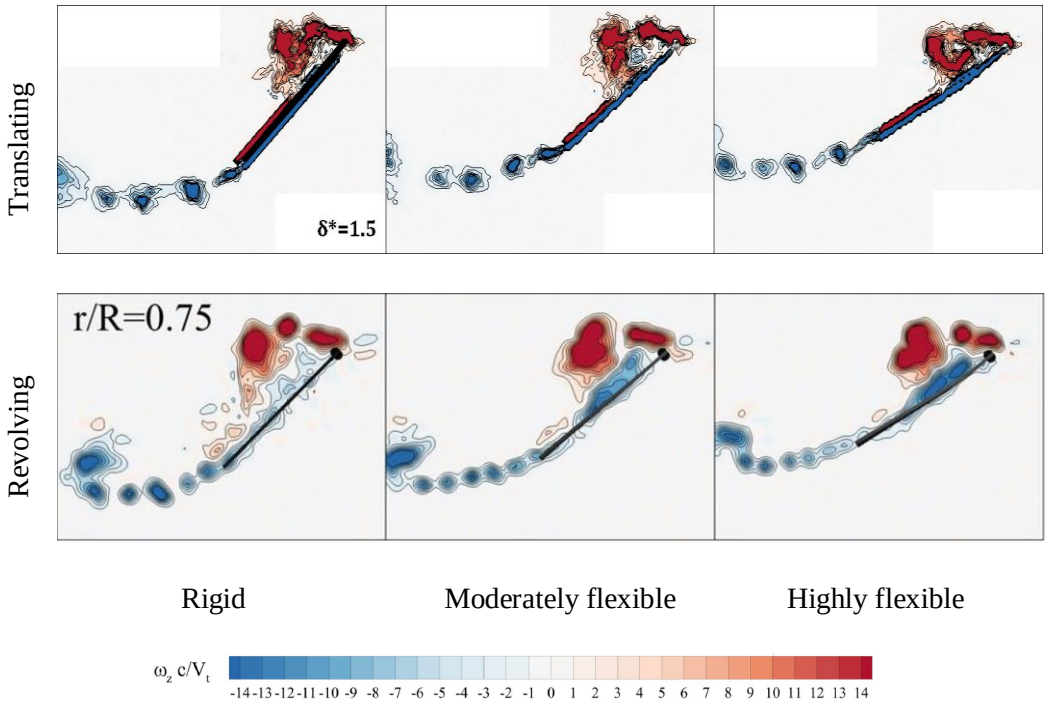

Figure 4.8. The out-of-plane vorticity contours for δ*=1.5 with respect to the 75% span position. Top: Translating wings. Bottom: Revolving wings

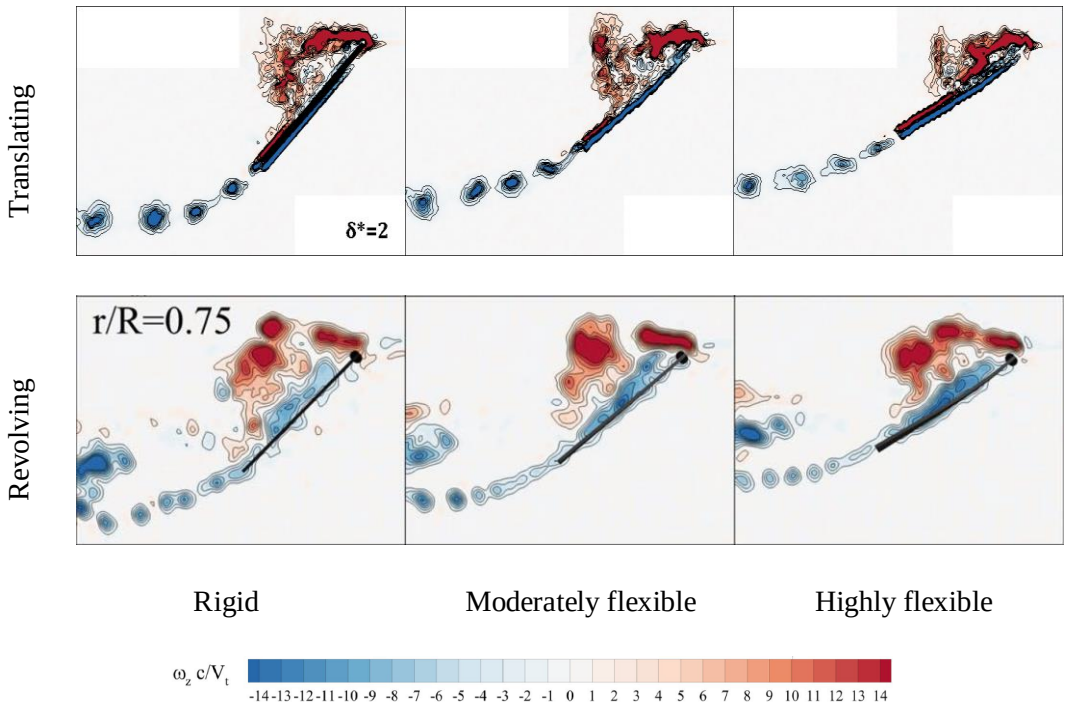

Figure 4.9. The out-of-plane vorticity contours for δ*=2.0 with respect to the 75% span position. Top: Translating wings. Bottom: Revolving wings

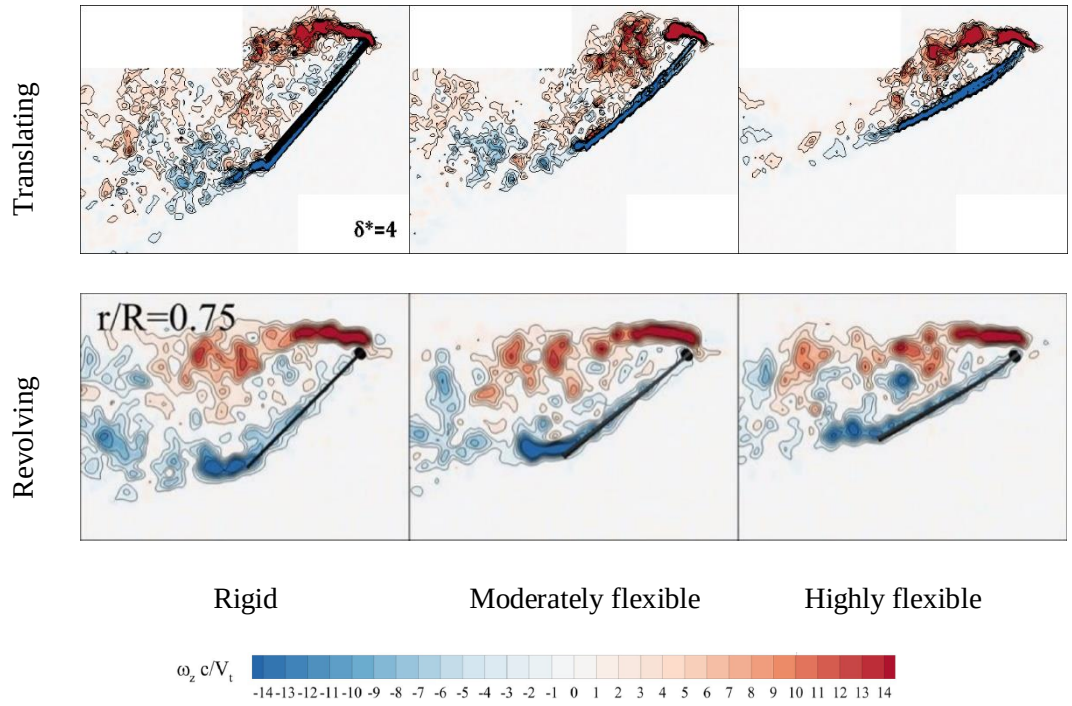

Figure 4.10. The out-of-plane vorticity contours for δ^*=4.0 with respect to the 75% span position. Top: Translating wings. Bottom: Revolving wings

The out of plane vorticity contours suggest similar vortex formations: a coherent LEV and a train of trailing edge vortices particularly at the initial phases of both motion kinematics and a chaotic flow field with an elongated incoherent positive vorticity layers emanating from the leading edge at a later phase (δ^*=4). At δ^*=4, the coherent LEV is burst into small-scale structures in both translating and revolving wings. Particularly in the case of rigid and moderately flexible wings, the shear layers emanating from the leading and trailing edges interact, and this interaction leads to small-scale vorticity pockets populating the wake. For the translating rigid and moderately flexible wings, the flow is completely detached from the wing surface; however, for the highly flexible wing, the flow that separates at the leading edge reattaches to the wing surface slightly before the trailing edge.

4.3. LEV Characteristics

4.3.1. LEV Circulation

In Figure 4.11, the temporal evolution of LEV circulation (Γ^*_{LEV}) for revolving and translating wings is given. Γ^*_{LEV} is the normalized LEV circulation. Γ^*_{LEV} is calculated for each phase of motion from rest to the final stage (δ^*=4). Note that, since the flow in translating motion is from left to right, the LEV has a clockwise vorticity resulting in negative values of circulation. In order to allow for a proper comparison with the revolving wing experiments and facilitate the interpretation of the results, the circulation values are multiplied by -1.

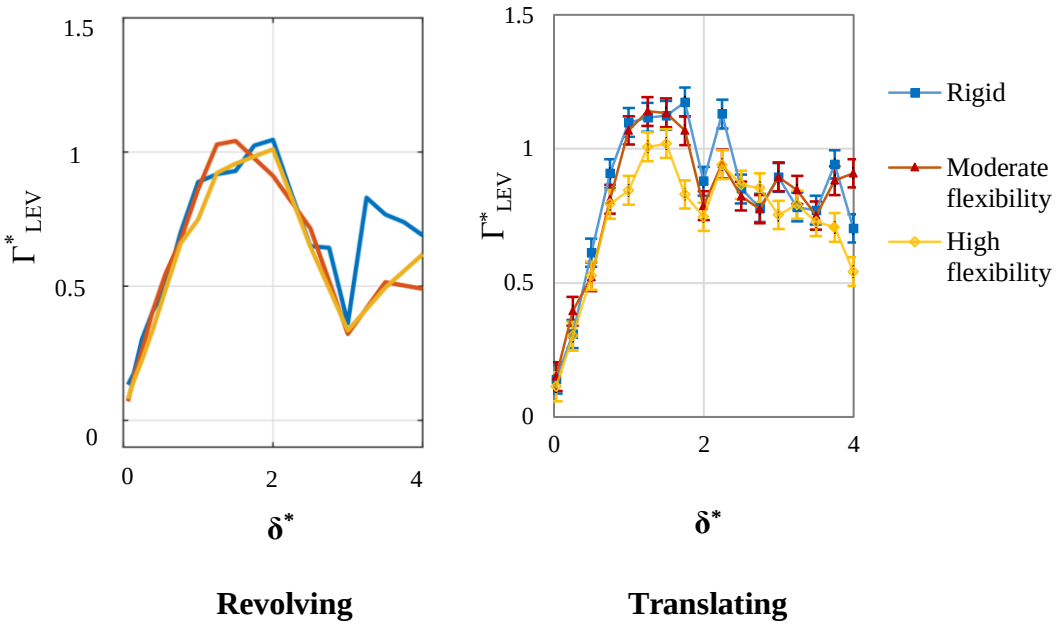

Figure 4.11. Temporal evolution of LEV circulation (Γ^*_{LEV}) for translating and revolving wings

Comparison of the temporal evolution of the LEV circulation between the rigid and flexible wings in the translating motion reveals that the rigid wing yields greater values of circulation particularly compared to the highly flexible wing. This difference in the circulation values stems from a larger LEV in the rigid wing case. The maximum LEV

circulation occurs at δ^*=1.75 in the rigid wing as a result of greater momentum given to the flow. The LEV bursts after δ^*=1.75 when circulation values decrease abruptly.

There are two prominent differences between the translating and revolving wings in terms of the normalized LEV circulation values. First, the translating motion yields greater circulation values, which is in accordance with the aforementioned hypothesis regarding the rotational accelerations playing role in the spanwise advection of vorticity and inhibiting excessive growth of the LEV. Second, the LEV circulation stays higher after δ^*=3 compared to the revolving wing case. However, this may be due to the shortcoming of the vortex core detection strategy in the detection of the LEV boundaries since it contradicts with the findings of Ol and Babinsky (2016) regarding the higher force generation of the revolving wings for an extended period of motion compared to the translating wings.

4.3.2. Evolution of TEV Circulation at Initial Stages of Motion

According to the Kelvin's circulation theorem, the circulation around a closed curve moving with the fluid remains constant with time ($\frac{D\Gamma}{Dt}$=0) (Anderson, 2011). Trailing edge vortex circulation is calculated for the initial stages of the translation motion ($\delta^* \leq 1.25$) in order to compare with the LEV circulation values. Such a comparison may allow for assessing the presence of the bound circulation under the assumption of two-dimensional flow around the wings at the early stages (Percin and van Oudheusden, 2015). In an earlier study, Pitt Ford and Babinsky (2013) showed that most of the circulation is contained in the LEV and the bound circulation remains small for a translating flat-plate airfoil at a fixed angle of attack of 15°. Percin and van Oudheusden (2015) also reported a similar behavior for a revolving flat-plate wing at an angle of attack of 45°. In this study, comparison of the LEV and TEV circulation values (Figure 4.12) suggests that there has to be a bound circulation or another source of circulation in the same sense with the TEV for the Kelvin's circulation theorem to be satisfied. This major difference may also be due to three-dimensionality of the flow even at early stages of the motion, which requires three-dimensional information

around the wings. As a bottom-line, in order to draw some conclusions regarding the presence of the bound circulation, further measurements at a number of planes at different spanwise stations and scrutiny of the three-dimensional flow fields are required. Note that, since the flow in translating motion is from left to right, the TEV has a counter-clockwise vorticity (positive values of circulation) and the LEV has a clockwise vorticity resulting in negative values of circulation. In order to allow for a proper comparison, the LEV circulation values are multiplied by -1.

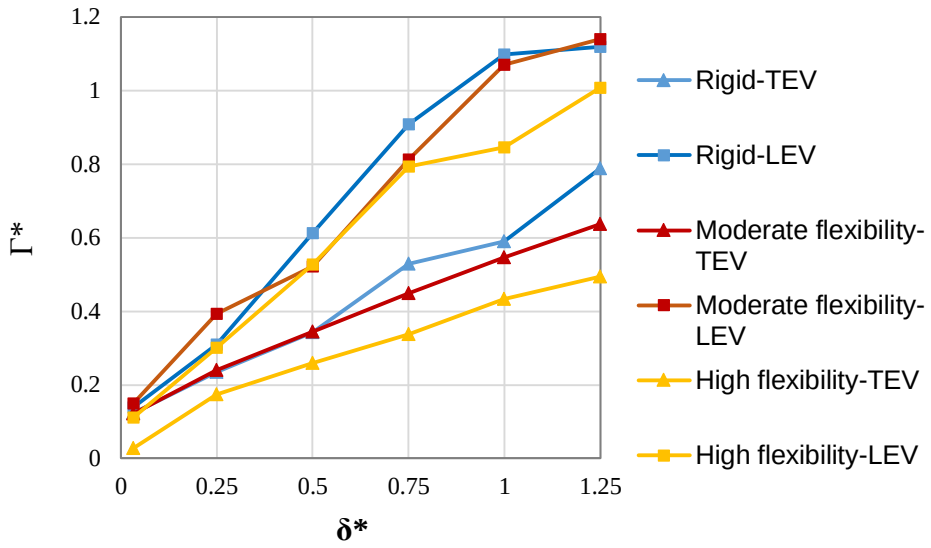

Figure 4.12. Temporal evolution of LEV circulation (Γ^*_{LEV}) and TEV circulation (Γ^*_{TEV}) in initial stages of motion (note that the LEV circulation values are multiplied by -1 to facilitate the comparison)

4.3.3. LEV Position

In this study, the vortex centroid is tracked by use of γ_1 integral method. Since the cameras are moving with the wing models, there is no need to subtract the convection velocity of the vortex. The first LEV is tracked for all stages of motion. In Figure 4.13, the temporal evolution of the LEV centroid in x and y directions are shown for translating (right side) and revolving wings (left side). It can be observed that in the

acceleration phase, the LEV centroid in all cases have a same trajectory to a greater or lesser extent. For rigid and moderately flexible wings, the vortex centroid cannot be detected after 1.75 chords traveled due to the burst of the LEV. In highly flexible wing, the LEV remains attached to the wing surface as a result of the wing deflection, and a smaller geometric angle of attack. The LEV in highly flexible case travels in a small range in the y direction, whereas the LEV in two other cases move continuously downward. In the moderately flexible wing, the LEV moves faster and travels more than the LEV in two other cases. The effect of high flexibility can be observed in the retention of LEV closer to the wing surface. In general, the LEV in translating motions is expected to be shed, and the rigid and moderately flexible wings prove this statement; however, the effect of high flexibility leads to the stability of the LEV in the highly flexible case.

The temporal evolution of the LEV centroid displays a similar trend for both motion kinematics. The major difference in this respect is that the LEV stays at a lower location (y/c) with respect to the leading edge and continuously move away in the vertical direction in the case of the translating wing while it stays at a more-or-less fixed location in the case of the revolving wing. The LEV rises and stays at a higher position with respect to the leading edge in the revolving wings, while in the translating wings, it always stays at a relatively lower position.

Temporal evolution of LEV centroid normal distance from the wing surface (s/c) for translating and revolving wings is shown in Figure 4.14. In both cases, the LEV stays closer to the wing surface in the case of the highly flexible wing. This may also boost force production due to the associated low pressure region (van de Meerendonk et al., 2018). However, it should also be noted that the LEV circulation and hence the magnitude of the associated low-pressure region is relatively low for the highly flexible wing due to decreased geometric angle of attack.

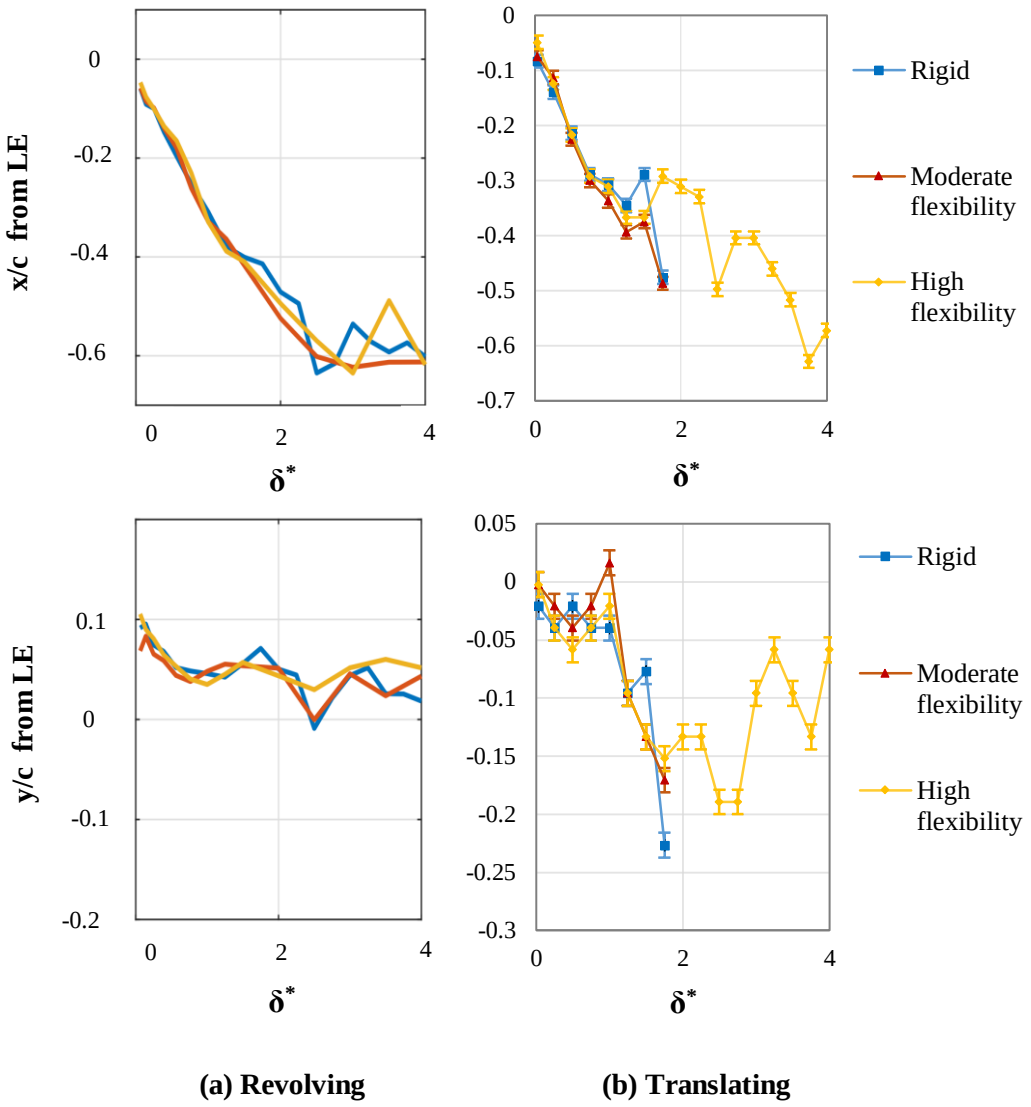

Figure 4.13. Temporal evolution of the LEV centroid. Top: Chord distance in x-direction from LE. Bottom: Chord distance in y-direction from the LE.

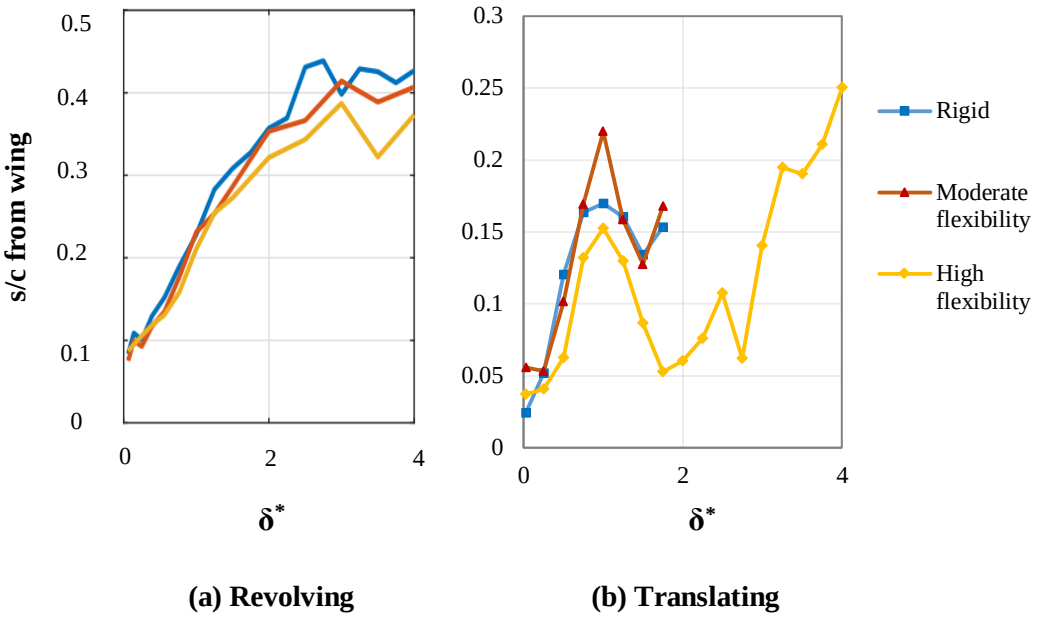

Figure 4.14. Temporal evolution of LEV centroid distance from the wing surface. Left: Revolving wings. Right: Translating wings

Schematic representation of the wing position with respect to the leading edge in x/c and y/c coordinates is shown in Figure 4.15. Note that the direction of the horizontal axis was selected to have a proper comparison with revolving-wings results.

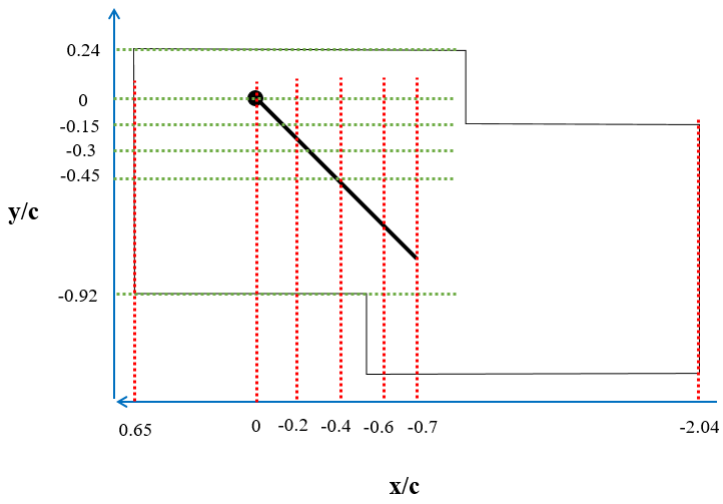

Figure 4.15. Schematic representation of the wing position with respect to the leading edge

CHAPTER 5

CONCLUSION

This study investigates the effect of wing flexibility on the flow structures around the surging-translating wings. The results of this study are compared with results of a study and TU Delft in which the wing models were investigated in a surging-revolving motion. The flow fields generated by translating low aspect ratio flat plate with different chordwise flexural stiffness have been investigated experimentally by 2D2C particle image velocimetry. Three different wings were tested to investigate the effect of flexibility; two flexible wing models and a rigid wing. The rigid wing is made of 1 mm thick Plexiglas, the moderately flexible wing and highly flexible wing are made of PET with thickness of 175 μm and 125 μm, respectively. The motion kinematics consists of two phases, the acceleration phase and the constant velocity phase. The wings start to accelerate from the rest to reach to the pre-defined terminal velocity over one chord length of travel. The wings continue to translate for more than three chord lengths in the second phase of motion.

The comparison of geometric angle of attack in the translating flexible wings reveals that the highly flexible wing deforms more than the moderately flexible one and presumably the force vector is tilted more towards the lift direction due to relatively lower geometric angle of attack. This can be a beneficial effect of flexible wings on the force generation, resulting in higher L/D. In translating moderately flexible wing, the geometric angle of attack is the same at starting and ending stages of the constant velocity phase. In the highly flexible wing, the geometric angle of attack decreases continuously during the motion resulting in higher deflection of the wing.

The comparison between the geometric angle of attack in translating and revolving wings (see Figure 4.2) reveals that the geometric angle of attack at 75% of span

position of translating wings is smaller than that of the revolving wings. This is attributed to smaller deformation of the revolving wing associated with the curvilinear nature of the motion.

The comparison of flow field around the translating wings reveals that the highly flexible wing generates less chaotic flow in the wake of the wing compared to two other cases. The LEV stays closer to the wing in highly flexible case as a result of the deformation of the wing and decreased geometric angle of attack.

The comparison between the results of this study with the revolving wings study revealed that the vortex structures have similar behavior in the acceleration phase of both cases. In the subsequent stages, the wings have similar chaotic flow in the wake in both cases; however, the highly flexible wing in the translating motion generates less chaotic flow due to the reattachment of the flow which leaves the TE tangentially. In the translating rigid and moderately flexible wings, the flow cannot reattach completely to the wing surface and the LEV sheds to the wake.

The LEV circulation in translating motion have same behavior with different values. The LEV circulation was shown that is a slightly higher in the translating cases comparing to the revolving wings. This may be due to rotational accelerations that plays role in the convection of vorticity in the spanwise direction in the revolving wings. The LEV circulation drops in the translating wings after $\delta^*=1.75$ and in the revolving wings after $\delta^*=2$; however, it stays higher after $\delta^*=3$ in the translating cases.

The comparison of the LEV and TEV circulation values in translating wings shows that there has to be another source of circulation or a bound circulation in the same sense with TEV for the Kelvin's circulation theorem to be satisfied. The three-dimensionality of the flow in the translating motion even at initial stages of motion can be the reason of this difference, which requires three-dimensional investigation of the flow around the wings at different spanwise stations.

The LEV centroid positions are similar for all wings in the acceleration phase, and they follow different path in the constant velocity phase of motion. The vortex centroid

detection method showed that the LEV is burst in the rigid and moderately flexible wings undergoing the linear translating motion after 1.75 chords traveled and cannot be detected; however, the LEV in the highly flexible wing keeps its coherency due to the deflection of the wing, and thus smaller geometric angle of attack. The result of this study showed that the effect of high flexibility mediates the LEV.

In both revolving and translating highly flexible wings, the LEV remains close to the wing surface which may result in force production enhancement due to associated lower pressure region. Decrease in geometric angle of attack results in lower LEV circulation and the magnitude of the associated low-pressure region which also has an effect on the force production.

The LEV in the revolving motion rises, and stays almost higher than the LE position, while in the translating wings, the LEV is always in a lower position. The LEV in highly flexible case rises after three chord lengths of travel, and reaches to the initial vertical position with respect to the LE.

Some recommendations for future works are listed as below:

- With the available setup, the planar flow was investigated which can be developed to a three-dimensional investigation in future works.
- By optimization of the driven system to be able to move at a higher speed, and having the ability to perform revolving motions, the possibility of further investigations will be provided.
- Stiffeners with different thicknesses and orientations can be added to the flexible wings to study flapping-flight aerodynamics more accurately.
- Plunging and pitching motions can be added to the motion kinematics to investigate flapping-wings in different maneuvers.
- Force measurement can be performed to investigate the effects of flexibility on the aerodynamic forces to arrive to the optimum wing models.

- Designing and manufacturing ornithopters is an interesting area in flapping-wing aerodynamics, and designing an agile insect inspired robot can be one of the interesting works in the future.

REFERENCES

Anderson, J. (2011). Fundamentals of Aerodynamics. Anderson series. McGraw-Hill.

Alexander, D. (2002). *Nature's flyers.* Johns Hopkins University Press.

Beals, N., & Jones, A. R. (2015). Lift production by a passively flexible rotating wing *AIAA Journal*, 53(10), 2995-3005.

Birch, J. M., & Dickinson, M. H. (2001). Spanwise flow and the attachment of the leading-edge vortex on insect wings. *Nature*, 412(6848), 729.

Birch and Dickinson. (2003). The influence of wing-wake interactions on the production of aerodynamic forces in flapping flight. *The Journal of Experimental Biology*, 206(13): 2257–2272.

Brossard, C., Monnier, J. C., Barricau, P., Vandernoot, F. X., Le Sant, Y., Champagnat, F., & Le Besnerais, G. (2009). *Principles and applications of particle image velocimetry*.

Combes, S. A., & Daniel, T. L. (2003). Flexural stiffness in insect wings I. Scaling and the influence of wing venation. *Journal of experimental biology*, 206(17), 2979-2987.

Denny, M. W. (1993). *Air and water: the biology and physics of life's media*. Princeton University Press.

Eldredge, J. D., Toomey, J., & Medina, A. (2010). On the roles of chordwise flexibility in a flapping wing with hovering kinematics. *Journal of Fluid Mechanics*, 659, 94-115.

Ellington, C. P. (1984). The aerodynamics of hovering insect flight. II. Morphological parameters. Philosophical Transactions of the Royal Society of London. B, Biological Sciences, 305(1122), 17-40.

Ellington, C. P., Van Den Berg, C., Willmott, A. P., & Thomas, A. L. (1996). Leading-edge vortices in insect flight. Nature, 384(6610), 626.

Graftieaux, L., Michard, M., & Grosjean, N. (2001). Combining PIV, POD and vortex identification algorithms for the study of unsteady turbulent swirling flows. *Measurement Science and technology*, 12(9), 1422.

Jardin, T., & David, L. (2014). Spanwise gradients in flow speed help stabilize leading-edge vortices on revolving wings. *Physical Review E*, 90(1), 013011.

Jardin, T., & David, L. (2015). Coriolis effects enhance lift on revolving wings. *Physical Review E*, *91*(3), 031001.

Jones, A. R., & Babinsky, H. (2010). Unsteady lift generation on rotating wings at low Reynolds numbers. *Journal of Aircraft*, 47(3), 1013-1021.

Lentink, D., & Dickinson, M. H. (2009). Rotational accelerations stabilize leading edge vortices on revolving fly wings. Journal of Experimental Biology, 212(16), 2705-2719.

Miller, L. A., & Peskin, C. S. (2009). Flexible clap and fling in tiny insect flight. *Journal of Experimental Biology*, 212(19), 3076-3090.

Mountcastle, A. M. & Daniel, T. L. (2009). Aerodynamic and functional consequences of wing compliance. *Animal Locomotion*, 46(5), 873-882.

Muijres, F. T., Johansson, L. C., Barfield, R., Wolf, M., Spedding, G. R., & Hedenström, A. (2008). Leading-edge vortex improves lift in slow-flying bats. *Science*, 319(5867), 1250-1253.

Ol, M. V., & Babinsky, H. (2016, January). Unsteady flat plates: a cursory review of AVT-202 research. In *54th AIAA Aerospace Sciences Meeting*.

Percin, M., & Van Oudheusden, B. W. (2015). Three-dimensional flow structures and unsteady forces on pitching and surging revolving flat plates. *Experiments in Fluids*, 56(2), 47.

Percin, M. (2015). Aerodynamic Mechanisms of Flapping Flight. *Doctoral dissertation, Delft University of Technology*.

Pines, D. J., & Bohorquez, F. (2006). Challenges facing future micro-air-vehicle development. *Journal of aircraft*, 43(2), 290-305.

Pitt Ford CW, Babinsky H (2013). Lift and the leading-edge vortex. *Journal of Fluid Mechanics*, 720, 280-313.

Sane, S. P. (2003). The aerodynamics of insect flight. *Journal of experimental biology*, *206*(23), 4191-4208.

Shyy, W., Aono, H., Chimakurthi, S. K., Trizila, P., Kang, C. K., Cesnik, C. E., & Liu, H. (2010). Recent progress in flapping wing aerodynamics and aeroelasticity. *Progress in Aerospace Sciences*, 46(7), 284-327.

Van de Meerendonk, R (2016). Three-dimensional flow and load characteristics of flexible revolving wings at low Reynolds number. *Master thesis, Delft University of Technology*.

Van de Meerendonk, R., Percin, M., & van Oudheusden, B. W. (2018). Three-dimensional flow and load characteristics of flexible revolving wings. *Experiments in Fluids*, 59(10), 161.

Van Den Berg, C., & Ellington, C. P. (1997). The three–dimensional leading–edge vortex of a ‘hovering’model hawkmoth. *Philosophical Transactions of the Royal Society of London. Series B: Biological Sciences*, *352*(1351), 329-340.

Wagner, H. (1925). Über die Entstehung des dynamischen Auftriebes von Tragflügeln. *ZAMM-Journal of Applied Mathematics and Mechanics/Zeitschrift für Angewandte Mathematik und Mechanik*, *5*(1), 17-35.

Weis-Fogh, T. (1973). Quick estimates of flight fitness in hovering animals, including novel mechanisms for lift production. *Journal of experimental Biology*, 59(1), 169-230.

Westerweel, J., & Scarano, F. (2005). Universal outlier detection for PIV data. *Experiments in fluids*, 39(6), 1096-1100.

Zhao, L., Huang, Q., Deng, X., & Sane, S. P. (2009). Aerodynamic effects of flexibility in flapping wings. *Journal of the Royal Society Interface*, 7(44), 485-497.